REPORT DOCUMENTATION PAGE

AFRL-SR-AR-TR-04-

0503

1. REPORT DATE (DD-MM-YYYY)	2. REPORT TYPE Final Report	3. DATES COVERED (From - To) Mar 2001 - Sep 2004

4. TITLE AND SUBTITLE	5a. CONTRACT NUMBER
Oxidation and Catalytic Efficiency of ZrB2 and HfB2 Based Ultra-High-Temperature Ceramic (UHTC) Composites Exposed to Supersonic Air Plasma	
	5b. GRANT NUMBER
	F49620-01-C-0026
	5c. PROGRAM ELEMENT NUMBER

6. AUTHOR(S)	5d. PROJECT NUMBER
Dr. Jochen Marschall	
	5e. TASK NUMBER
	5f. WORK UNIT NUMBER

7. PERFORMING ORGANIZATION NAME(S) AND ADDRESS(ES)	8. PERFORMING ORGANIZATION REPORT NUMBER
Molecular Physics Laboratory SRI International 333 Ravenswood Avenue Menlo Park CA 94025-3493	

9. SPONSORING/MONITORING AGENCY NAME(S) AND ADDRESS(ES)	10. SPONSOR/MONITOR'S ACRONYM(S)
USAF/AFRL AFOSR 801 N. Randolph Avenue Arlington VA 22203	AFOSR
	11. SPONSOR/MONITOR'S REPORT NUMBER(S)

12. DISTRIBUTION/AVAILABILITY STATEMENT

Distribution Statement A. Approved for public release; distribution is unlimited.

20041008 217

13. SUPPLEMENTARY NOTES

14. ABSTRACT

This report summarizes the activities and results of experimental and modeling activities performed for the Air Force Office of Scientific Research (AFOSR) under Contract F49620-01-C-0026, "Oxidation and Catalytic Efficiency of ZrB2 and HfB2 Based Ultra-High-Temperature Ceramic (UHTC) Composites Exposed to Supersonic Air Plasma."
The goals of this project were to (1) experiimentally investigate UHTC oxidation in a supersonic oxidizing flow environment, (2) develop oxidation models that could be incorporated into aerothermal heating and trajectory codes, and (3) experimentally characterize the catalytic efficiency of UHTC samples for surface recombination of dissociated oxygen and nitrogen. Given the importance of impact damage to the leading edges of hypersonic vehicles, a task was added during the third year of the project to (4) begin preliminary high-velocity impact experiments on UHTC materials. Research efforts and accomplishments in each of these four areas are summarized below.
The results of this research have led to eight presentations at various conferences and meetings, and have been written up in three technical publications 1-3. Manuscripts of these technical papers are included in this report as Appendixes I, II, and III.

15. SUBJECT TERMS

16. SECURITY CLASSIFICATION OF:			17. LIMITATION OF ABSTRACT	18. NUMBER OF PAGES	19a. NAME OF RESPONSIBLE PERSON
a. REPORT	b. ABSTRACT	c. THIS PAGE			
U	U	U	UU	63	19b. TELEPHONE NUMBER (Include area code)

SRI International

Annual Performance and Final Report • September 2004

Oxidation and Catalytic Efficiency of ZrB_2 and HfB_2 Based Ultra-High-Temperature Ceramic (UHTC) Composites Exposed to Supersonic Air Plasma

Prepared by:

Dr. Jochen Marschall
Molecular Physics Laboratory
SRI International

Prepared for:

Dr. Joan Fuller
Director, Ceramics and Nonmetallic Materials Program
AFOSR/NA
801 North Randolph Street, Room 732
Arlington, VA 22203-1977

INTRODUCTION

This report summarizes the activities and results of experimental and modeling activities performed for the Air Force Office of Scientific Research (AFOSR) under Contract F49620-01-C-0026, "Oxidation and Catalytic Efficiency of ZrB_2 and HfB_2 Based Ultra-High-Temperature Ceramic (UHTC) Composites Exposed to Supersonic Air Plasma."

The goals of this project were to (1) experimentally investigate UHTC oxidation in a supersonic oxidizing flow environment, (2) develop oxidation models that could be incorporated into aerothermal heating and trajectory codes, and (3) experimentally characterize the catalytic efficiency of UHTC samples for surface recombination of dissociated oxygen and nitrogen. Given the importance of impact damage to the leading edges of hypersonic vehicles, a task was added during the third year of the project to (4) begin preliminary high-velocity impact experiments on UHTC materials. Research efforts and accomplishments in each of these four areas are summarized below.

The results of this research have led to eight presentations at various conferences and meetings, and have been written up in three technical publications [1-3]. Manuscripts of these technical papers are included in this report as Appendixes I, II, and III.

SUMMARY OF EFFORTS AND ACCOMPLISHMENTS

Surface Catalysis Experiments [2]

During hypersonic flight, shock waves that form ahead of leading edges can dissociate molecular species in the atmosphere. These dissociated species can migrate to the surface of the vehicle, where they may participate in exothermic surface reactions. Recombination reactions of O+O and N+N release energies of about 5.2 eV (500 kJ/mol) and 9.8 eV (950 kJ/mol), respectively. When these reactions take place on a surface, a portion of this energy can be transferred directly to the surface as heat. The contributions of surface-catalyzed recombination reactions to aerothermal heating have been demonstrated, for example, by flight experiments conducted on the base heat shield of the Space Shuttle Orbiter [4-6].

At moderate temperatures, surface recombination efficiency can be determined using a diffusion tube side-arm reactor coupled with laser-induced fluorescence (LIF) species detection diagnostics. Molecular species, O_2 or N_2, are dissociated using a microwave discharge on the main flow tube. As the flow passes the entrance to a dead-end side-arm tube, atomic species diffuse down the tube and recombine on the walls. Under steady-state conditions a decaying atom profile, which can be measured using LIF, is established along the axis of the side-arm tube. The catalytic efficiency of a surface is described by the recombination coefficient, which is defined as the fraction of atomic collisions with the surface that remove the atom from the gas phase. Recombination coefficients are determined by matching measured atom profiles to numerical solutions of the appropriate diffusion-reaction equation. The facility, experimental procedures, and data analysis techniques have been described in detail in several publications.[7-9]

1

Such measurements were completed for HfB_2 - 20v/o SiC (A-7) and ZrB_2 - 20v/o SiC (A8) samples for O-atom and N-atom recombination over a temperature range from about 295 K to 1000 K. The two major findings of this study were:[2]

(i) The efficiency of ZrB_2/SiC and HfB_2/SiC composites for recombining dissociated oxygen and nitrogen can be non-negligible between room temperature and 1000 K, with maximum observed recombination coefficients of $\sim 5 \times 10^{-2}$, a value comparable to those of oxidized aerospace alloys like Inconel 617 and one to two orders of magnitude larger than for typical silica-based coatings like the reaction cured glass (RCG) coating on the Space Shuttle.[10]

(ii) Repeated testing shows that the catalytic efficiency of UHTC materials can be altered by interactions with the environment even at relatively low temperatures; in particular, surface oxidation—in this case the formation of B_2O_3—appears to lower the catalytic efficiency below that of the virgin material.

A detailed description of the experiments and results was published in a paper titled "Catalytic Atom Recombination on ZrB_2/SiC and HfB_2/SiC Ultrahigh-Temperature Ceramic Composites," published in the Journal of Spacecraft and Rockets, Vol. 41, No. 4, (2004), pp. 576-581. A reprint of this paper is attached as Appendix I to this report.

Laboratory-Scale Arc-Jet Testing

A significant portion of the proposed research effort was to modify an existing laboratory-scale arc-jet, previously used for diamond deposition experiments, as a test facility for exposing UHTC materials to supersonic oxidizing gas flows. This involved installing a new roots blower pumping system to maintain relevant stagnation and chamber pressures, adding a new view port and a two-color pyrometer to monitor sample surface temperatures, designing and constructing an integrated water-cooled arc-jet nozzle and sample insertion stage, and assembling a data acquisition system. Figure 1 shows photographs of the arc-jet facility at SRI International.
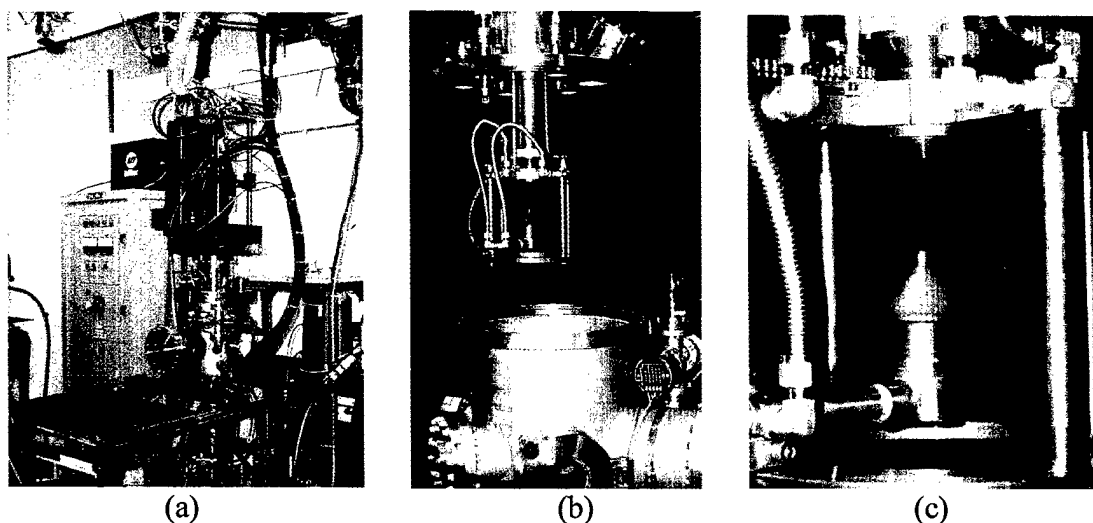

(a) (b) (c)

Figure 1. (a) Arc-jet facility; (b) integrated, water-cooled arc-jet nozzle and sample insertion stage; (c) close-up of nozzle and sample insertion stage.

2

The integrated arc-jet nozzle and sample insertion stage was constructed from oxygen-free copper parts. Cooling channels were machined into individual parts and the parts were joined with silver solder. Test specimens were inserted into a conical graphite holder mounted in a water-cooled copper swing arm. The swing arm was spring-loaded to position the sample on centerline with the nozzle. Samples could be moved in and out of the flow manually.

The arc-jet nozzle itself was adapted from a commercial oxygen cutting torch head (Hypertherm MAX200). The cutting torch head is intended to function in a transferred-arc mode, where electrons leave the cathode and exit the nozzle to strike a grounded metal work-piece. The cutting torch head was modified for the arc-jet by grounding the nozzle. The arc is then confined within the head, with electrons leaving the cathode and striking the interior of the nozzle near the exit. The gas is heated as current flows through a gap between the cathode and the nozzle, creating a plume of energetic gas that flows into the vacuum chamber and over the test sample at supersonic speed. This is shown schematically in Fig. 2a. A UHTC sample in the arc-jet stream is shown in Fig. 2b.
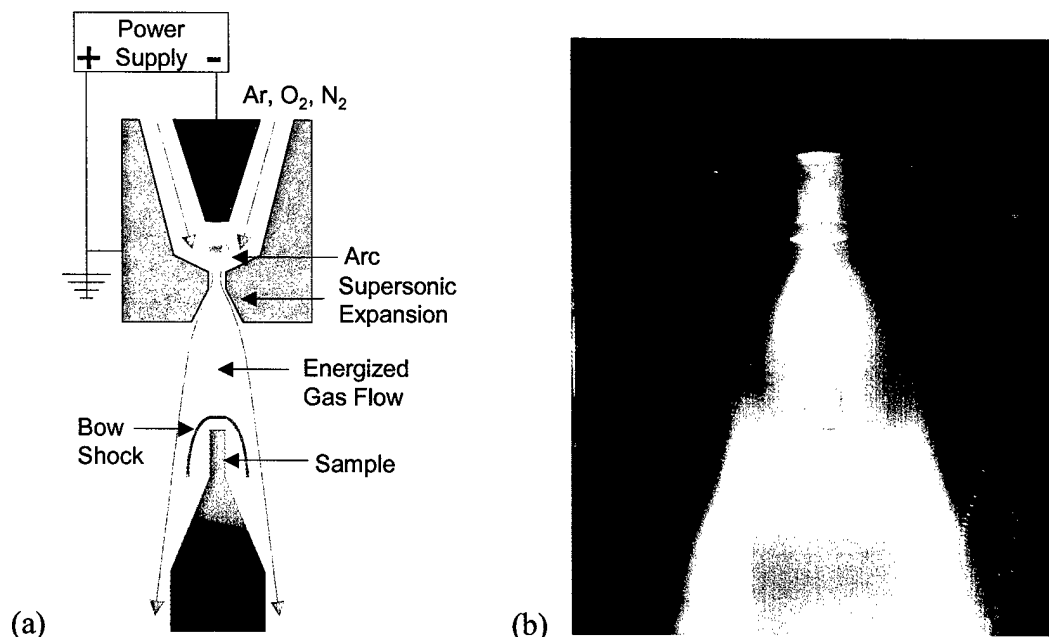

Figure 2. (a) Diagram of arc-jet and test sample, and (b) UHTC cap exposed to arc-jet plume

The arc-jet facility was made operational at the end of the second project year. Numerous tests of the facility have been run using different mixtures of argon, air, oxygen, and nitrogen. Most runs use a standard mixture of 15 standard liters per minute (slm) Ar, with or without the addition of 0.2 slm O_2. With this flow mixture, the system demonstrated operation at an arc power of 1.0-1.3 kW, with a maximum stream enthalpy of 2-3 MJ/kg and background chamber pressure around 0.5 Torr. Various carbon, HfB_2-20v/oSiC, ZrB_2-20 v/o SiC, and ZrB_2-14v/oSiC-30v/oC specimens have been exposed to the arc-flow. UHTC test specimens were either in the form of solid, flat-faced cylinders or thin discs that capped carbon tubes.

3

We conducted a variety of diagnostic measurements under these conditions. Specimens experienced surface temperatures up to 2000 K, as measured with a Mikron M90 two-color pyrometer. The addition of oxygen to the flow consistently raised surface temperatures by several hundred degrees Kelvin. A special probe with the same dimensions as the test specimens was constructed to measure stagnation pressure. It consisted of a graphite cylinder with a ~ 0.020" orifice on the surface, inserted into the graphite sample holder. The probe was connected via stainless-steel tubing to a Baratron pressure gauge. Stagnation point pressures around 2.5 Torr were measured for the standard operating conditions. A similar probe, consisting of a graphite tube with a graphite or UHTC cap, was constructed to estimate surface heat flux using an energy balance approach. This measurement indicated stagnation point heat fluxes of about 100 W/cm^2.

Figure 3 shows an example of a ZrB_2-14v/oSiC-30v/oC UHTC sample exposed for ~12 minutes to the low-pressure, supersonic arc-jet plume under standard oxidizing conditions. Surface temperatures ranged between 1800 and 2000 K during the run. Zone C of the cylindrical specimen is inside the sample holder and not directly exposed to the flow. Zone B shows signs of melt formation, indicating the oxidation of surface boride and carbide phases to an oxide glass. Zone A, closest to the leading edge, shows no surface melt layer, presumably because in this region the high surface temperature, low ambient pressure, and high shear stresses combine to remove any SiO_2/B_2O_3 melt that may form. Energy dispersive x-ray analysis (EDX) confirmed the depletion of carbon and the enhancement of oxygen in zones A and B.
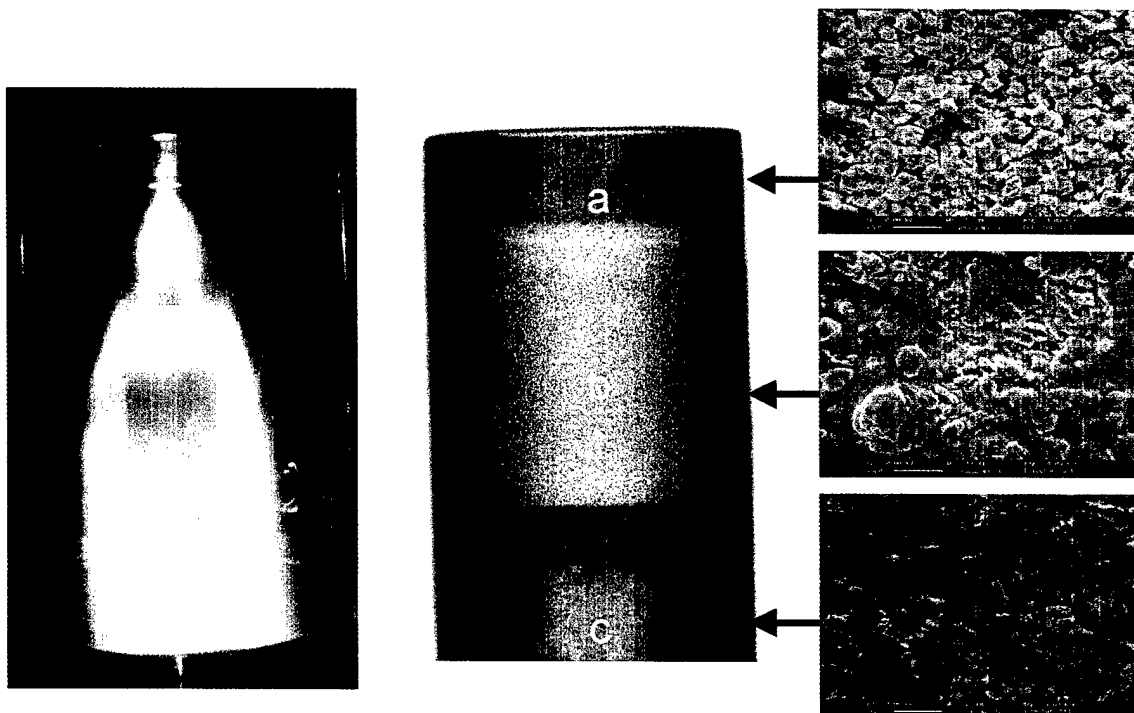

Figure 3. UHTC specimen (ZrB_2-14v/oSiC-30v/oC) exposed to the arc-jet flow under standard conditions. Zone C inside sample holder; zone B shows signs of surface melt; zone A is depleted in carbon and shows no surface SiO_2 melt layer melt.

4

At this stage of development, we have demonstrated the operation of a laboratory-scale arc-jet capable of generating supersonic, low-pressure, oxidizing flows sufficiently energetic to elevate UHTC surface temperatures to ~2000 K and cause observable oxidation and melt formation in minutes.

Unfortunately, we have also encountered a significant electrode erosion problem, which in turn often leads to unacceptable levels of surface contamination on the faces of our test samples. Such contamination affects surface properties (emittance, catalytic efficiency) and interferes with surface analytic examinations of the UHTC oxide. This contamination problem caused us to postpone extensive oxidation testing at this time, so that we may conserve UHTC specimens for future experiments in a cleaner facility.

As an alternative to the arc-jet, we diverted some of our efforts to setting up a complementary test environment for UHTC materials, focused especially on the influence of dissociated oxygen on UHTC oxidation. The test facility uses a 6-kW microwave discharge, formerly used to dissociate semiconductor-processing gases for cleaning and etching operations, to generate gas streams with high concentrations of atomic oxygen. These activated gas streams are flown over UHTC specimens heated in a tube furnace. The facility is shown in Fig. 4.

Initial experiments with silicon wafers have shown dramatic increases in passive oxidation at relatively low temperatures (~900 C), as can be seen in Table 1. In Fig. 5, the classical Deal-Grove model for silicon oxidation[11] is fit to last data group listed in Table 1. The extracted parabolic rate constant B is 85 times larger than typical for oxidation by molecular oxygen under similar temperature and pressure conditions.
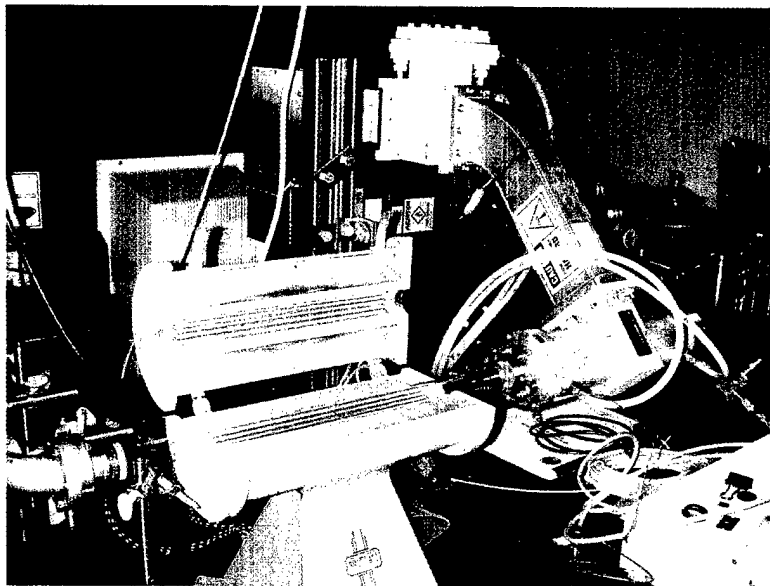

Figure 4. Microwave discharge test facility.

Table 1. (100) Silicon oxidation experiments

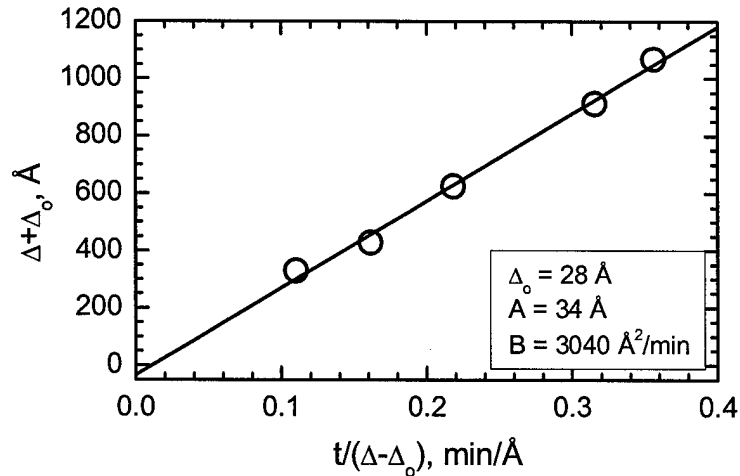| Type	Gas Mixture, (%)	Downstream Pressure, (Torr)	Time, (min)	Discharge	Oxide Thickness, (Å)
p	$87O_2$-13Ar	3.2	180	off	59
p	$87O_2$-13Ar	3.2	180	on	742
p	$83N_2O$-17Ar	3.4	180	on	1120
n	$87O_2$-13Ar	4.7	180	off	65
n	$87O_2$-13Ar	4.8	180	on	1114
n	$78N_2O$-22Ar	4.9	180	on	1381
n	$87O_2$-13Ar	3.3	30	on	301
n	$87O_2$-13Ar	3.25	60	on	400
n	$87O_2$-13Ar	3.25	124	on	596
n	$87O_2$-13Ar	3.2	270	on	884
n	$87O_2$-13Ar	3.2	360	on	1039

Figure 5. Fit of the Deal-Grove oxidation model to n-type (100) Si samples oxidized for different times at ~910 °C.

We are extending these experiments to higher temperatures, to other silica formers (SiC and Si_3N_4) and then to UHTC composites, under a recently funded NSF grant.

Oxidation Model Development [1]

Oxidation is a dynamic process, sensitive to perturbations in temperature and oxidant concentration. It is coupled to the flow environment both chemically and thermally. For the interpretation of transient test results, as produced for example by arc-jet exposure, and for the prediction of oxide formation during different flight conditions, a computational model of oxide formation and loss in an aeroconvective heating environment is highly desirable. Such a model must consider many different aspects: passive and active oxidation boundaries; oxidation rates;

6

transport of oxidants and reactants to the surface and to the oxide/substrate interface; changes in thermal and surface properties as a result of oxidation; and so on.

As a first step toward this goal, the PI and Y.-K. Chen of NASA Ames Research Center (ARC) have modified the FIAT thermal response code to track the formation of oxide layers on simple silica formers (e.g., Si, SiC) during exposure to transient oxidizing aerothermal heating environments[1]. The FIAT program was developed for computing one-dimensional energy transport in multilayer thermal protection systems that can ablate from the surface and decompose in depth.[12] FIAT uses finite volume discretization and an implicit numerical scheme to solve surface energy balance, internal energy balance, internal decomposition, and internal mass balance equations at each time step. The program accepts convective heat transfer boundary conditions specified in terms of heat transfer coefficients and recovery enthalpy at the wall, as usually employed for aerothermal heating simulations.

At each time step, for a given surface temperature and oxygen partial pressure at the wall, the modified FIAT program evaluates whether conditions favor passive or active oxidation. For the present work we have used the transition boundary presented by Balat et al.,[13,14] in their study of active and passive oxidation of silicon carbide. Under passive oxidation conditions, our oxidation model follows the classic Deal-Grove reaction-diffusion model,[11] where we consider interface reactions instantaneous, oxygen solubility constant, and oxide growth limited by temperature-dependent oxygen diffusion through the oxide scale. As the oxide layer grows, we change the thermal properties from substrate to oxide values, and compute hemispherical surface emittance as a function of oxide thickness and temperature using thin-film optics equations[15] followed by spectral integration over the Planck function.

We compute the gas phase composition at the wall using ACE, a thermochemistry code that computes the steady-state chemistry between a surface and its gas environment.[16] This equilibrium chemistry calculation is coupled with a surface mass balance that accounts for material leaving the surface as pyrolysis gases, ablation products, and thermo-mechanically failed material as well as for gaseous species diffusing in from the boundary layer edge. In the active oxidation regime, surface recession is computed using dimensionless mass flux (B') tables generated by ACE.

We have exercised this modified code for a SiC slab subjected to boundary conditions approximated from the atmospheric entry conditions for the HL-20 crew transfer vehicle trajectory, as presented by Saunders et al. [17]. Examples of computational results are shown below in Fig. 6. A more comprehensive description can be found in AIAA paper 2004-0485, presented at the 42nd, AIAA Aerospace Sciences Meeting and Exhibit, Reno, NV, 5-8, January 2004. [1] The full paper is included in this report as Appendix II.
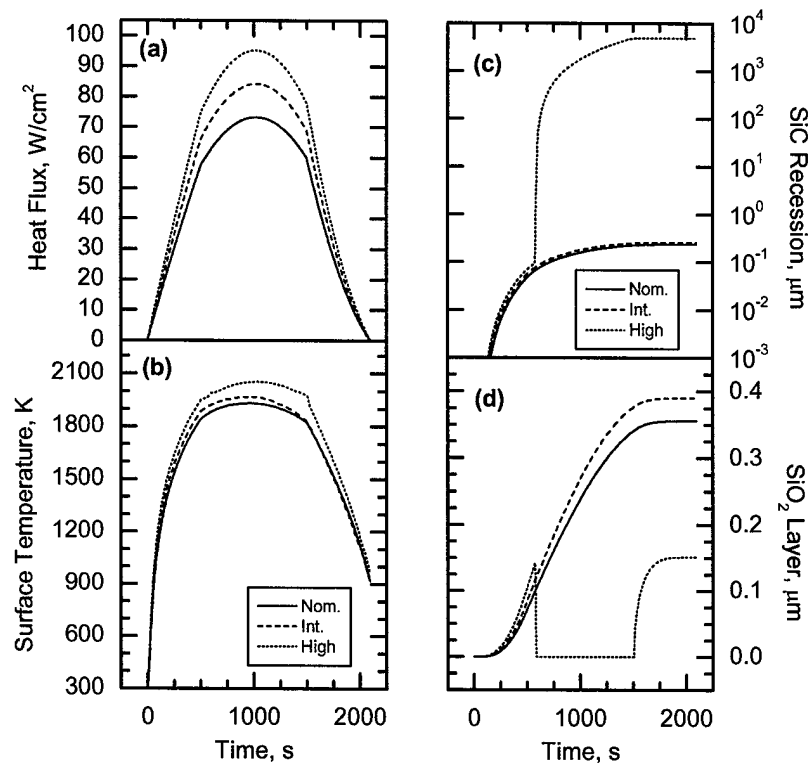
7

Figure 6. (a) Heat flux; (b) surface temperature, (c) SiC recession, and (d) SiO_2 growth.

High-Velocity Impact Experiments [3]

Impact damage is a major concern for any leading-edge component, since leading edges are exposed to the most severe aerothermal environments and directly influence vehicle flight characteristics. A very large spectrum of possible impacts exists, ranging from tool drops, to collisions with high-velocity debris during takeoff and landing, to hypervelocity impacts with micrometeorites and "space junk" in orbit. Very little information can be found in the literature on the impact resistance of UHTC materials; some data were recently obtained during the Next Generation Launch Technology program,[18] but they have not been published and the program has wound down.

Given the importance of the subject—highlighted by the Columbia Shuttle disaster—exploratory impact tests were initiated during the third year of this project. The tests sampled two regimes: velocities in the 100 – 350 m/s range using a compressed gas gun to fire stainless steel and tungsten carbide balls with diameters of 0.5 to 0.8 mm, and the 1-3 km/s range using a 2 MV Van de Graaff particle accelerator to fire micron-scale carbonyl iron particles.

The hypervelocity experiments, conducted at Concordia College, Moorhead, MN, produced insignificant surface damage to polished HfB_2-20v/oSiC and ZrB_2-20v/oSiC specimens. This result is thought to be due to the small mass of the fired iron particles, and the hardness differences between the UHTC materials and carbonyl iron, which causes a large fraction of the impact energy to be dissipated in plastic deformation and melting of the iron particle.

8

In the gas-gun experiments at SRI, impacts in the 100 to 300 m/s range with tungsten carbide (WC) balls produced surface patterns of ring and radial cracks typical of brittle materials under blunt indentors; an example is shown in Fig. 7a. Observed impact damage is consistent with elastic loading stresses. The ring cracks are the surface traces of Hertzian cone cracks propagating in-depth. Impressions are extremely shallow, with depth to sphere radius ratios of about 1 to 400. With increasing impact velocity, ring cracks appear first and radial cracks follow. Similar WC impacts generated more extensive cracking patterns on ZrB_2-20v/oSiC than on HfB_2-20v/oSiC. Stainless steel impacts produced no radial cracks and much less extensive ring cracking than WC impacts under similar conditions. Optical detection of cracking patterns required impact velocities of ~ 200 m/s; however, damage is likely at lower velocities.

During the fourth year of the project, additional impact tests were conducted at SRI on ZrB_2/20%SiC and HfB_2/20%SiC specimens provided by NASA ARC, as well as homogeneous and fibrous monolith ZrB_2/30%SiC samples provided by Professor Bill Fahrenholtz's group at the University of Missouri-Rolla. Figure 7b summarizes the outer ring crack diameters observed as a function of impact kinetic energy. If the outer ring crack diameters are taken as a measure of the distance from the impact at which the maximum radial tensile stress just exceeds the critical stress of the material, Fig. 7b suggests impact resistance is ordered HfB_2/20%SiC > ZrB_2/30%SiC > ZrB_2/20%SiC.
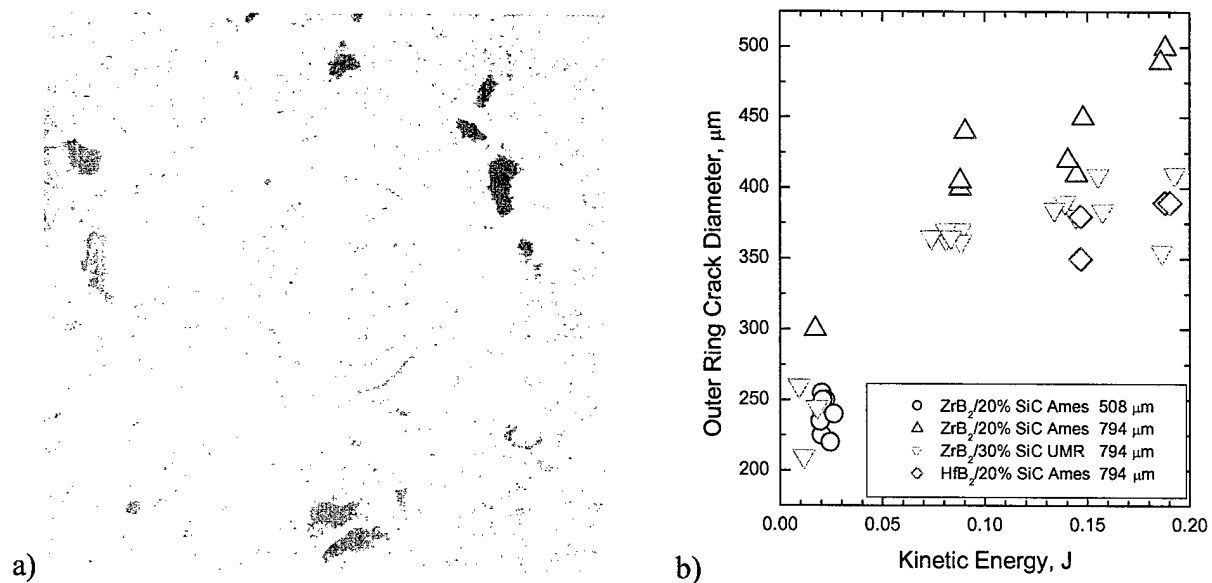

Figure 7. (a) Surface damage produced on a ZrB_2/20%SiC surface by the 308 m/s impact of a 794 μm diameter tungsten carbide ball; (b) outer ring crack diameters as a function of tungsten sphere kinetic energy at impact, for two sphere diameters and three different UHTC materials

We examined the effect of impact damage on HfB_2-20v/oSiC fracture strength by impacting several disc and type-B bend bar specimens with 0.8-mm-diameter WC balls. The discs were subsequently tested using a standard concentric ring flexural test as described in ASTM standard C 1499,[19] and bars were subsequently tested according to ASTM standard C 1161.[20] The

9

results are shown in Fig. 8. The decrease in fracture strength is significant, even at lower impact velocities, where damage is difficult to detect optically.
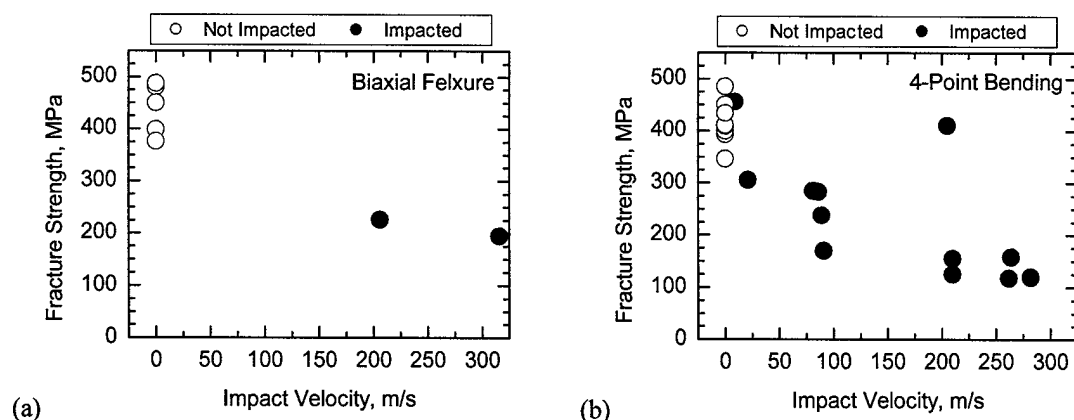

Figure 8. The effect of high velocity impact by a 794 μm (1/32") diameter tungsten carbide sphere on the fracture strength of HfB$_2$/20%SiC samples. (a) 2.54-cm-diameter discs tested in a biaxial flexure; (b) type B bend bars tested in four-point bending.

The major findings of this study are: (i) UHTC materials are hard and reasonably resistant to impacts by softer, more malleable materials (stainless steel, carbonyl iron); (ii) in the high-velocity impact regime, UHTC materials exhibit classic brittle material failure under impacts with hard, dense, brittle materials (tungsten carbide); and (iii) UHTC materials may sustain hard-to-detect impact damage that can significantly lower their fracture strength.

Details of the initial impact experiments can be found in the manuscript, "Microhardness and High-Velocity Impact Resistance of HfB$_2$/SiC and ZrB$_2$/SiC Composites," Journal of Materials Science, Vol. 39 (In Press, 2004), which is included in this report as Appendix III.

ACKNOWLEDGMENT/DISCLAIMER

ON-SITE PERSONNEL SUPPORTED

During the course of this project, the following SRI individuals received support from AFOSR Contract F49620-01-C-0026:

Jochen Marschall   PI, Research Scientist, Molecular Physics Laboratory

Christopher Morgan   Postdoctoral Fellow, Molecular Physics Laboratory

Don Eckstrom   Senior Staff Scientist, Applied Physics Division

David Erlich	Physicist, Materials Research Laboratory
William Olson	Engineering Assistant, Molecular Physics Laboratory
Steve Young	Electronics Technician, Molecular Physics Laboratory

In addition, Nader Moussa and Núria Queraltó contributed to this project as summer students, supported by the NSF Research for Undergraduates program and the SRI Academy, respectively.

PUBLICATIONS

Marschall, J., D. C. Erlich, H. Manning, W. Duppler, D. Ellerby, and M. Gasch, "Microhardness and High-Velocity Impact Resistance of HfB_2/SiC and ZrB_2/SiC Composites," *Journal of Materials Science*, In Press, 2004.

Marschall, J., A. Chamberlain, D. Crunkleton, and B. Rogers, "Catalytic Atom Recombination on ZrB_2/SiC and HfB_2/SiC Ultra-High Temperature Ceramic Composites," *Journal of Spacecraft and Rockets*, Vol. 41, No. 4, 2004, pp. 576-581.

Marschall, J. and Y.-K. Chen, "Modeling Surface Oxidation in Transient Aerothermal Heating Environments," AIAA 2004-0485, January 2004

INTERACTIONS/TRANSITIONS

SRI has established working scientific collaborations with research groups at the University of Missouri – Rolla (Professors William Fahrenholtz and Gregory Hilmas), Concordia College (Professor Heidi Manning), and Vanderbilt University (Professor Bridget Rogers.) In addition, we have maintained strong interactions with the personnel in the Thermal Protection Materials and Systems Branch at NASA Ames Research Center.

The results of this work led to the following talks/presentations:

1. Presented invited talk at the Materials and Manufacturing Directorate, AFRL WPAFB, November 7, 2001; "Oxidation and Catalytic Efficiency of ZrB_2 and HfB_2 Based Ultra-High Temperature Ceramic (UHTC) Composites Exposed to Supersonic Air Plasma." Also attended and presented a poster on the same topic at the Scientific Advisory Board Review Session.

2. Presented invited talk to NASA personnel in the Thermal Protection Materials and Systems Branch at NASA Ames Research Center: "UHTC Research in the Molecular Physics Laboratory at SRI International," September 25, 2002.

3. Attended and presented at the 27th Annual Conference on Composites, Materials, and Structures, Cocoa Beach, FL, January 27-30, 2003: "Catalytic Atom Recombination on ZrB_2/SiC and HfB_2/SiC Ultra-High Temperature Ceramic Composites"

4. Attended two technical interchange meetings (1/23/03 and 5/14/03) involving Lockheed-Martin and NASA Ames Research Center efforts to develop UHTC

materials for leading edges, as part of NASA's Next Generation Launch Technology and 2nd Generation Reusable Launch Vehicle programs.

5. Presented invited talk to NASA personnel in the Thermal Protection Materials and Systems Branch at NASA Ames Research Center; "Estimation of Temperature-Dependent Emittance from Room Temperature Spectral Reflectance Measurements," March 6, 2003.

6. Attended and presented a poster at the 55th Pacific Coast Regional and Basic Science Division Fall Meeting, The American Ceramics Society, Oakland, CA, October 19-22, 2003; "Catalytic Atom Recombination on ZrB_2/SiC and HfB_2/SiC Ultra-High Temperature Ceramic Composites."

7. Attended and presented talk at the AFOSR Workshop on Ultra-High-Temperature Ceramics, Wintergreen VA, November 5-7, 2003; "Response of UHTC Materials to Aerothermal Heating and Impact Loading."

8. Attended and presented talk at the 42nd Aerospace Sciences Meeting, Reno NV, January 5-8, 2004; "Modeling Surface Oxidation in Transient Aerothermal Heating Environments."

Preliminary O-atom oxidation experiments will be presented at the 2004 Joint International Meeting of the Electrochemical Society, October 3-8, Honolulu, Hawaii. Additional UHTC high-velocity impact data will be presented at the 29th International Conference on Advanced Ceramics and Composites, January 23-28, 2005, Cocoa Beach, Florida.

DISCOVERIES/INVENTIONS/PATENTS

None.

HONORS

None.

REFERENCES

1. J. Marschall and Y.-K. Chen, "Modeling Surface Oxidation in Transient Aerothermal Heating Environments," AIAA Paper 2004-0485 (January, 2004).

2. J. Marschall, A. Chamberlain, D. Crunkleton, and B. Rogers, "Catalytic Atom Recombination on ZrB_2/SiC and HfB_2/SiC Ultra-High Temperature Ceramic Composites," J. Spacecraft Rock., In Press (2004).

3. J. Marschall, D. C. Erlich, H. Manning, W. Duppler, D. Ellerby, and M. Gasch, "Microhardness and High-Velocity Impact Resistance of HfB_2/SiC and ZrB_2/SiC Composites," Journal of Materials Science, Accepted (2004).

4. J. V. Rakich, D. A. Stewart, and M. J. Lanfranco, "Results of a Flight Experiment on the Catalytic Efficiency of the Space Shuttle Heat Shield," AIAA Paper 82-0944 (1982).

5. D. A. Stewart, J. V. Rakich, and M. J. Lanfranco, "Catalytic Surface Effects Experiment on the Space Shuttle," AIAA Paper 81-1143 (1981).

6. D. A. Stewart, J. V. Rakich, and M. J. Lanfranco, "Catalytic Surface Effects on Space Shuttle Thermal Protection System during Earth Entry of Flights STS-2 through STS-5," NASA CP-2283 (March 1983).

7. D. A. Stewart, "Determination of Surface Catalytic Efficiency for Thermal Protection Materials - Room Temperature to Their Upper Use Limit," AIAA Paper 96-1863 (June 1996).

8. J. Marschall, "Experimental Determination of Oxygen and Nitrogen Recombination Coefficients at Elevated Temperature Using Laser-Induced Fluorescence," AIAA Paper 97-3879 (August, 1997).

9. S. Sepka, Y.-K. Chen, J. Marschall, and R. A. Copeland, "Experimental Investigation of Surface Reactions in Carbon Monoxide and Oxygen Mixtures," J. Thermo. Heat Trans. **14**, 45-52 (2000).

10. D. A. Stewart, "Surface Catalysis and Characterization of Proposed Candidate TPS for Access-to-Space Vehicles," NASA TM-112206 (July 1997).

11. B. E. Deal and A. S. Grove, "General Relationship for the Thermal Oxidation of Silicon," J. Appl. Phys. **36**, 3770-3778 (1965).

12. Y.-K. Chen and F. S. Milos, "Ablation and Thermal Response Program for Spacecraft Heatshield Analysis," J. Spacecraft Rock. **36**, 475-483 (1999).

13. M. Balat, G. Flamant, G. Male, and G. Pichelin, "Active to Passive Transition in the Oxidation of Silicon Carbide at High Temperature and Low Pressure in Molecular and Atomic Oxygen," Journal of Materials Science **27**, 697-703 (1992).

14. M. J. H. Balat, "Determination of the Active-to-Passive Transition in the Oxidation of Silicon Carbide in Standard and Microwave-Excited Air," Journal of the European Ceramic Society **16**, 55-62 (1996).

15. F. Abelès, "Optical Properties of Metallic Films," in *Physics of Thin Films*, M. H. Francombe and R. W. Hoffman, Eds. (Academic Press, New York, 1971), Vol. 6, pp. 151-204.

16. R. M. Kendall, "An Analysis of the Coupled Chemically Reacting Boundary Layer and Charring Ablator, Part V. A General Approach to the Thermochemical Solution of Mixed Equilibrium-NonequilibriumHomogeneous or Heterogeneous Systems," NASA CR-1064 (June 1968).

17. D. Saunders, G. Allen, P. Gage, and J. Reuther, "Crew Transfer Vehicle Trajectory Optimization," AIAA Paper 2001-2885 (June 2001).

18. LockheedMartin, "5.0 Damage Tolerance," presented at Next Generation Launch Vehicle Technology: UHTC Technical Interchange Meeting, NASA Ames Research Center, 2003.

19.   Anon., "Standard Test Method for Monotonic Equibiaxial Flexural Strength of Advanced Ceramics at Ambient Temperature," ASTM C 1499-03 (July, 2003).

20.   Anon., "Standard Test Method for Flexural Strength of Advanced Ceramics at Ambient Temperature," ASTM C1161-02c (October, 2002).

APPENDICES

Catalytic Atom Recombination on ZrB₂/SiC and
HfB₂/SiC Ultrahigh-Temperature Ceramic Composites

J. Marschall, A. Chamberlain, D. Crunkleton, and B. Rogers

Modeling Surface Oxidation in Transient Aerothermal Heating Environments

Jochen Marschall and Y.-K. Chen

Microhardness and High-Velocity Impact Resistance of HfB₂/SiC and ZrB₂/SiC Composites

J. Marschall, D. C. Erlich, H. Manning, W. Duppler, D. Ellerby, and M. Gasch

Catalytic Atom Recombination on ZrB$_2$/SiC and HfB$_2$/SiC Ultrahigh-Temperature Ceramic Composites

J. Marschall, A. Chamberlain, D. Crunkleton, B. Rogers

Catalytic Atom Recombination on ZrB₂/SiC and HfB₂/SiC Ultrahigh-Temperature Ceramic Composites

Jochen Marschall*
SRI International, Menlo Park, California 94025
Adam Chamberlain†
University of Missouri–Rolla, Rolla, Missouri 65409
and
Daniel Crunkleton‡ and Bridget Rogers§
Vanderbilt University, Nashville, Tennessee 37235

Results are presented of an experimental investigation into the efficiency of zirconium diboride/silicon carbide and hafnium diboride/silicon carbide ultrahigh-temperature ceramic composites for catalyzing the surface recombination of dissociated oxygen and nitrogen at moderate surface temperatures. Experiments were conducted with a diffusion-tube side-arm reactor, together with laser-induced fluorescence species detection diagnostics. Experiments reveal recombination coefficients in the range between silica glasses and oxidized metals, as well as evidence of environment-induced surface modification.

Introduction

ULTRAHIGH temperature ceramic (UHTC) composites based on zirconium diboride (ZrB₂) and hafnium diboride (HfB₂) are promising materials for use as sharp leading-edge components on hypersonic flight vehicles. Both the diborides and their primary metal oxides have extremely high melting points.[1] UHTC composites have shown good dimensional stability in low-pressure supersonic aerothermal heating environments, where other refractory materials rapidly fail by melting, spalling, pyrolyzing, or ablating.[2] Several studies have demonstrated that the high-temperature oxidation/ablation resistance of diboride-based UHTC materials is enhanced by the addition of silicon carbide (SiC).[3–7] Two promising formulations are known as A-7, with a nominal composition of HfB₂ with 20-vol% SiC and A-8, with a nominal composition of ZrB₂ with 20-vol% SiC. These formulations were flown during the slender hypervelocity aerothermodynamic research probe flight experiments, SHARP B1[8,9] and SHARP B2. (Details of the SHARP B1 and B2 flight experiments are available at http://asm.arc.nasa.gov/.)

One aspect of UHTC performance not previously investigated is the catalytic efficiency of ZrB₂/SiC and HfB₂/SiC composites for recombining dissociated oxygen and nitrogen. During hypersonic flight through Earth's atmosphere, high-temperature shock waves form in front of vehicle leading edges. Molecular oxygen and nitrogen, with respective dissociation energies of approximately 5.2 eV (500 kJ/mol) and 9.8 eV (950 kJ/mol), can dissociate in these extreme environments. If the resulting atomic species diffuse to the vehicle surface and recombine there, this dissociation energy becomes available, and some fraction may go directly to the surface as heat. The importance of surface catalyzed reactions to Earth entry heating has been demonstrated in a series of flight experiments on NASA's Space Shuttle Orbiter.[10–12]

*Research Scientist, Molecular Physics Laboratory; jochen.marschall@sri.com. Senior Member AIAA.
†Graduate Student, Department of Ceramics Engineering.
‡Assistant Professor, Department of Chemical Engineering.
§Postgraduate Researcher, Department of Chemical Engineering.

Many studies of oxygen and nitrogen recombination have been done on a variety of different structural and thermal protection system materials. However, no experimental data exist for UHTC materials or their oxides. UHTC materials are intermetallic compounds with unique chemical and electrical properties; their catalytic performance may differ substantially from those of pure metals or pure ceramics that have been tested in the past. It is also evident that the catalytic behavior of UHTC materials under transient, high-temperature plasma exposures must be closely coupled with development of oxide layers. Generally, metals have been found to catalyze oxygen and nitrogen recombination much more efficiently than ceramics. It is believed that the catalytic efficiency of a material is related to its intrinsic electronic transport properties. In their virgin state, UHTC composites have an electrical resistivity of ∼10–20 $\mu\Omega \cdot$ cm at room temperature, a range comparable to that of many iron alloys. As in metals, the resistivity of virgin UHTC materials increases linearly with increasing temperature. However, once a surface oxide forms, this metal-like behavior will change. B₂O₃ and SiO₂ are covalently bonded insulators, and ZrO₂ and HfO₂ are ionic compounds. The intrinsic electrical conductivity of these materials is much less than that of the virgin UHTC materials. The electrical transport mechanisms are also different. In the case of B₂O₃ and SiO₂, semiconductorlike transport is generated by impurities that can create p- or n-type doping, whereas for ZrO₂ and HfO₂, electrical conductivity is dominated by oxygen ion diffusion. It appears that oxygen recombination is more favorable on p-type semiconducting surfaces.[13,14] The n- or p-type nature of the amorphous silica and boron oxides in UHTC oxide layers has not been experimentally determined, and no data on oxygen or nitrogen recombination on ZrO₂ or HfO₂ surfaces were found in the literature.

Here, we present the results of a first experimental investigation into the efficiency of ZrB₂/SiC and HfB₂/SiC composites for catalyzing the recombination of dissociated oxygen and nitrogen. The present study is focused on a moderate temperature regime (from room temperature to 1000 K) that can be accessed by the use of a diffusion-tube side-arm reactor technique. We find recombination efficiencies that lie in the range between silica glasses and oxidized metals, as well as evidence of environment-induced oxidation that modifies the catalytic efficiency.

Materials and Methods

Side-Arm Reactor Facility

Surface catalysis experiments were conducted in a diffusion-tube side-arm reactor. The theory of surface catalysis measurements in
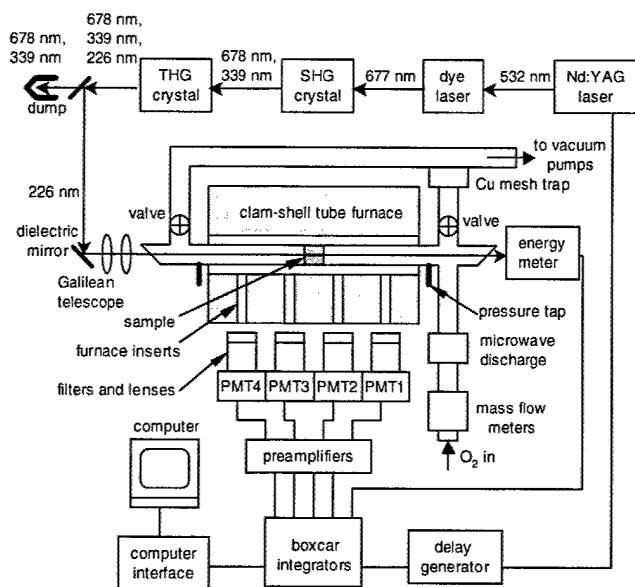
Fig. 1 Diagram of diffusion-tube side-arm reactor facility.

a diffusion-tube side-arm reactor, as well as the side-arm reactor facility, has been described in a number of publications.[15–17] Here we give only a brief overview of the equipment and test procedures. A diagram of the facility is shown in Fig. 1.

The reactor consists of a Pyrex® main flow tube and a quartz deadend side-arm tube attached via a cross. A 46-cm length of the side-arm tube was enclosed in a clam-shell tube furnace capable of reaching ~1500 K. Molecular gases are introduced into the upstream side of the flow tube and exhausted downstream with a turbomolecular pump backed with a roughing pump. A microwave cavity positioned upstream of the cross was used to dissociate a fraction of the molecular gas to produce either O or N atoms. As the atomic species diffuse down the side-arm tube, they recombine on the walls. Under steady-state conditions, a decaying atom concentration profile is established along the axis of the side-arm tube. The shape of this profile is determined by the catalytic activity of the reactor walls. Their catalytic efficiency is parameterized by the recombination coefficient γ, defined as the fraction of atomic collisions with the surface that remove an atom from the gas phase. Recombination coefficients are determined by matching measured atom concentration profiles to numerical solutions of the appropriate reaction–diffusion equation.[15,18,19]

Measurements of the (relative) atom concentration are made as a function of axial position along the side-arm tube using two-photon laser-induced fluorescence (LIF). In this process, atoms are excited with two photons of ultraviolet light and monitored by their subsequent fluorescence in the near infrared. Ultraviolet (UV) light, at wavelengths of ~226 nm for two-photon O-atom excitation and ~207 nm for two-photon N-atom excitation, is generated by frequency tripling red light produced by a Continuum ND60 dye laser. Frequency tripling is achieved using two beta-barium borate crystals for second and third harmonic generation. Red light at ~678 nm is produced using LDS 698 laser dye, and red light at ~621 nm is produced using Rhodamine 640 laser dye; both dyes are dissolved in methanol. The dye laser is pumped with the frequency-doubled output (~532 nm green light) from a Continuum NY81 Nd:YAG laser.

The UV laser light is directed through a collimating Galilean telescope and then through a quartz Brewster angle window down the centerline of the side-arm tube by the use of dichroic mirrors. A Molectron energy meter is used to monitor fluctuations in the laser pulse energy as the beam exits the side-arm tube through a second Brewster angle window on the cross. Atom fluorescence is monitored at right angles to the side-arm tube through quartz-lined optical access ports in the furnace by the use of four gated Hamamatsu R636 photomultiplier (PMT) tubes spaced ~8.9 cm apart. The PMTs are fitted with narrow-band interference filters, with a bandwidth of

~3 nm, centered at 845 nm for O-atom fluorescence and 745 nm for N-atom fluorescence. Signals from the energy meter and the PMTs were sent to a Stanford Research Systems data acquisition system consisting of a preamplifier, several boxcar integrators, and a computer interface module. The laser and data acquisitions system were synchronized at 10 Hz by the use of a Stanford Research Systems delay generator.

Surface Catalysis Test Samples

UHTC billets were provided by the NASA Ames Research Center, from material stock manufactured during the SHARP B1 and B2 programs. The as-pressed cylindrical billets were ~7.6 cm in height and ~7.6 cm in diameter. Catalysis test samples, in the form of 2.1-cm-long tubes with an outer diameter of 2.0 cm and a wall thickness of 0.28 cm were machined from a single disk cut from each billet. The test samples where machined by the use of techniques similar to those employed in the manufacture of SHARP B1 and SHARP B2 flight components. Electrical discharge machining (EDM) was used to cut the disks from the billets and the tubes out of the disks. Diamond grinding of the inner tube surfaces was used to achieve final dimensions.

After machining, the samples were rinsed with methanol, cleaned in an ultrasonic bath for ~15 min in a water–detergent mixture, rinsed in distilled water, and then air dried. After being loaded into the side-arm reactor, samples were conditioned under vacuum for at least 12 h before testing. This was done to remove residual, loosely bound volatiles from surfaces without heating and to provide a uniform initial condition for all experiments. In actual application, UHTC materials may be subjected to a variety of environmental contaminates, for example, water, salts, and hydrocarbons, the ramifications of which must be addressed in separate experiments.

Surface Catalysis Measurements

Three types of measurements were done as part of the UHTC surface catalysis experiments. First, the relative signal response of the four PMTs was determined by turning the diffusion tube into a flow tube. Under flow tube conditions, wall losses are minimized and each PMT should see fluorescence from similar atom concentrations. With small corrections for concentration differences due to surface recombination and pressure gradients, as well as the pressure dependence of the fluorescence yield, the relative sensitivity of each PMT can be determined and used to normalize diffusion tube data. Second, diffusion tube measurements were made to determine the recombination coefficients of quartz tube inserts. These data were analyzed with a classic exponential decay model.[18] Third, diffusion tube experiments were made to determine the recombination coefficients of UHTC samples. UHTC samples were placed within the quartz tube inserts and positioned at the midpoint of the furnace-enclosed side-arm tube. A three-section diffusion tube model was used to extract recombination coefficients from the measured data.[15] In this model, the recombination coefficients of the first and third tube sections were fixed at the measured quartz values, and the tube diameter was fixed at the quartz tube insert value.

Surface catalysis testing proceeded in a cyclical manner. Before and after each UHTC sample was tested, the LIF signal normalization was confirmed through flow-tube measurements and the recombination coefficients of the quartz sample tubes were measured as a function of temperature in diffusion tube experiments. Each UHTC sample was tested on three different days, at several discreet temperatures, with multiple measurements at each temperature. During the first test run, measurements were made at 295, 473, and 673 K; during the second test run these measurements were repeated and extended to 923 K; and during the third test run these measurements were repeated once more. The reactor was not opened between runs, and the samples remained continuously under vacuum.

Surface Analysis Samples

The UHTC samples used for catalysis testing are not easily probed by surface analysis techniques because of their tubular shape. A second set of samples was prepared in the form of ~1-cm² squares

Table 1   Test conditions seen by the 10 A-7 and A-8
UHTC surface analysis specimens

Gas environment	Run 1[a]	Run 2[b]
Vacuum	1,2	2
300 mtorr oxygen (discharge off)	3,4	4
300 mtorr oxygen (discharge on)	5,6	6
300 mtorr nitrogen (discharge off)	7,8	8
300 mtorr nitrogen (discharge on)	9,10	10

[a]Ramp to 673 K, hold 4 h, cool under vacuum.
[b]Ramp to 673 K, hold 2 h, ramp to 923 K, hold 2 h, cool under vacuum.

from scrap material remaining from the manufacture of the catalysis samples. These scraps were thin (~2–4 mm thick) cross sections of material cut by EDM directly adjacent to the catalysis sample disks within the billets. The faces nearest the catalysis sample disks were polished to a mirror finish with diamond grit, and individual coupons were cut from the polished cross sections with a diamond cutting wheel. At least 12 samples of each UHTC composition were obtained in this way. The samples were rinsed with methanol, cleaned in an ultrasonic bath, and air dried before insertion into the side-arm reactor.

Surface Analysis Sample Exposures

The surface analysis samples were positioned with their polished side facing up in the side-arm tube at the same nominal location as the catalysis samples and exposed to a variety of gas and heating conditions (Table 1). During run 1 heating cycles, two samples at a time were heated to 673 K, held for 4 h at temperature, and then cooled under vacuum. After cooling, one of the samples was removed. The remaining sample was exposed to the run 2 heating cycle, which consisted of heating to 673 K, holding at temperature for 2 h, heating to 923 K, holding at temperature for 2 h, and then cooling under vacuum. These heating cycles are similar to those seen by the surface catalysis samples, though not identical. After exposure, samples were stored at ambient temperature and atmospheric conditions until surface analysis. Several additional samples were left untested to serve as unexposed standards for comparison.

Surface Analyses

Samples were examined with energy dispersive x-ray (EDX) analysis and x-ray photoelectron spectroscopy (XPS). The EDX analyses were performed with a LEO-435VP scanning electron microscope operated at 20 kV, with an Oxford EDX system fit with a SiLi detector. XPS analyses were performed in a hemispherical analyzer-based system (Leybold-Heraeus, LH 18) with Al K_α (1486.6 eV) x rays and a 45-deg takeoff angle.

The EDX technique samples material to a depth of several micrometers with a lateral resolution of several 100 μm. The XPS technique probes only near-surface material to a depth of several nanometers with lateral resolution of ~1 mm.

Results

The results of the side-arm reactor experiments are the measured recombination coefficients shown in Figs. 2–6. The averaged recombination coefficient values for the quartz sample tubes are also included in the Figs. 2, 3, 5, and 6 for comparison to the UHTC values. The melting point T_m of crystalline B_2O_3 is indicated in each of Figs. 2, 3, 5, and 6. Its significance will be discussed in the Discussion section. The data demonstrate an interesting, history-dependent behavior that suggests that UHTC surfaces are modified during testing.

Oxygen Surface Recombination

The measured oxygen recombination coefficients for the A-8 and A-7 materials are shown in Figs. 2 and 3, respectively. The following behavior is observed for the ZrB_2, 20-vol% SiC sample in Fig. 2. During the first test, recombination coefficients of ~1 × 10^{-3}–2 × 10^{-3} are found at room temperature. On heating to
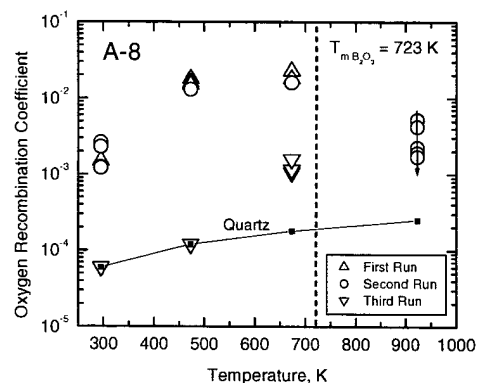
Fig. 2   Oxygen recombination coefficient of A-8 (ZrB_2, 20-vol% SiC) UHTC specimen.
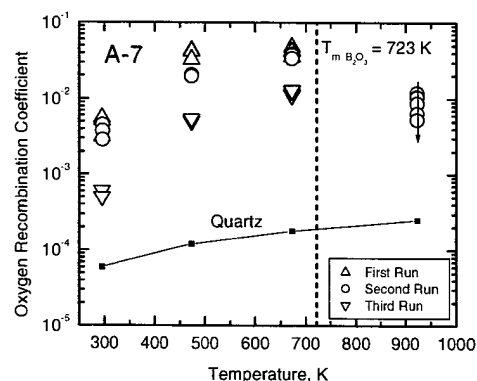
Fig. 3   Oxygen recombination coefficient of A-7 (HfB_2, 20-vol% SiC) UHTC specimen.
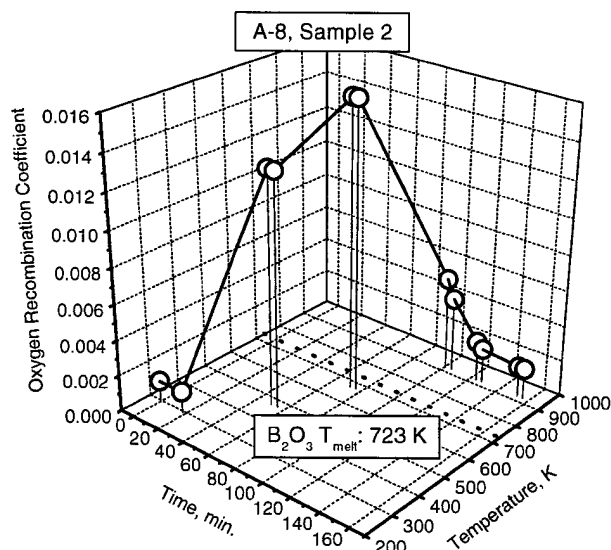
Fig. 4   Measured oxygen recombination coefficients for the A-8 (ZrB_2, 20-vol% SiC) UHTC specimen during the second test run; connecting line serves as a visual guide only.

473 K, the recombination coefficients rise by an order of magnitude to ~1 × 10^{-2}–2 × 10^{-2}. With further heating to 673 K, they increase slightly to the ~2 × 10^{-2}–3 × 10^{-2} range. During the second test, the measured recombination coefficients at each of these temperatures are substantially the same as in the first test (with some experimental scatter). When the sample is heated to 923 K, we observe a steady decrease in catalytic efficiency with time. This is indicated by the downward arrow in Fig. 2, and can be seen more clearly in Fig. 4, which plots the measured recombination coefficient as a function of
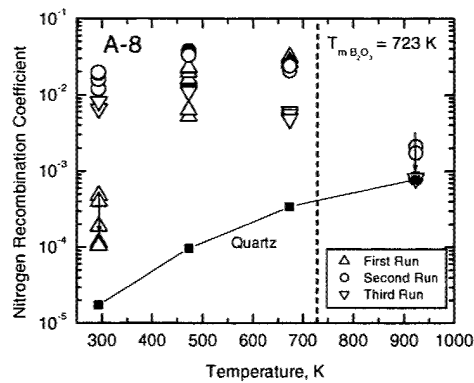
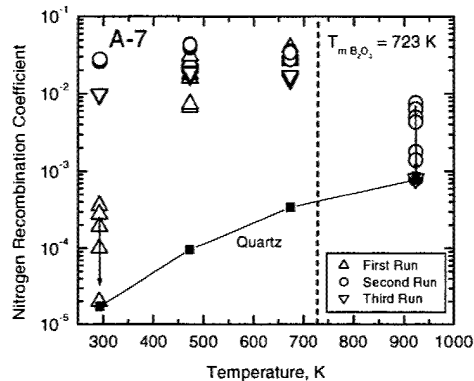Fig. 5 Nitrogen recombination coefficient of A-8 (ZrB$_2$, 20-vol% SiC) UHTC specimen.

Fig. 6 Nitrogen recombination coefficient of A-7 (HfB$_2$, 20-vol% SiC) UHTC specimen.

Fig. 7 EDX analysis of run 2 A-7 (HfB$_2$, 20-vol% SiC) specimens, showing peak intensity vs x-ray energy over the range 0–2 keV: nitrogen (0.392 keV), oxygen (0.525 keV), and hafnium (1.28 keV) peaks are highlighted by bars; O/Hf peak ratios are indicated for each panel.

time and temperature. During the third test, the sample's catalytic efficiency for O-atom recombination is drastically reduced, by one to two orders of magnitude. In fact, the recombination coefficients of the UHTC sample cannot be distinguished from those of the quartz sample tubes at the two lowest test temperatures.

The same basic phenomena are seen in Fig. 3 for the HfB$_2$, 20-vol% SiC sample: reproducible recombination coefficient values at 295, 473, and 673 K during the first two tests, a steady decrease in catalytic efficiency with time at 923 K, and lower recombination coefficient values at the lower test temperatures on retesting. The recombination coefficients are somewhat higher overall and do not decrease as much after heating at 923 K; however, the trends observed for the HfB$_2$, 20-vol% SiC sample are clearly similar to those seen for the ZrB$_2$, 20-vol% SiC sample.

Nitrogen Surface Recombination

The measured nitrogen recombination coefficients for A-8 and A-7 are shown in Figs. 5 and 6, respectively, along with the averaged values for quartz. Distinctly different behavior is observed when the tests are conducted under dissociated nitrogen.

The initial room temperature recombination coefficients of the A-8 sample steadily decrease with time, reaching values of around 1×10^{-4}. These values increase to the 1×10^{-2}–3×10^{-2} range at 473 and 673 K. On the second test run, the room temperature recombination coefficients are no longer at 1×10^{-4} but are two orders of magnitude higher. The measurements at 473 and 673 K are in reasonably good agreement with those obtained on the first run. The measurements made at 923 K show a steady decline in recombination efficiency with time, eventually making the UHTC specimens indistinguishable from the quartz side-arm tube. The third run shows recombination coefficients of order 1×10^{-2} at room temperature, 473 K, and 673 K, in agreement with the results of the second run, though generally somewhat lower. At 923 K, the recombination coefficient is again indistinguishable from the quartz.

Similar behavior is seen for the A-7 specimen in Fig. 6, with an initial decrease in recombination efficiency toward the quartz value
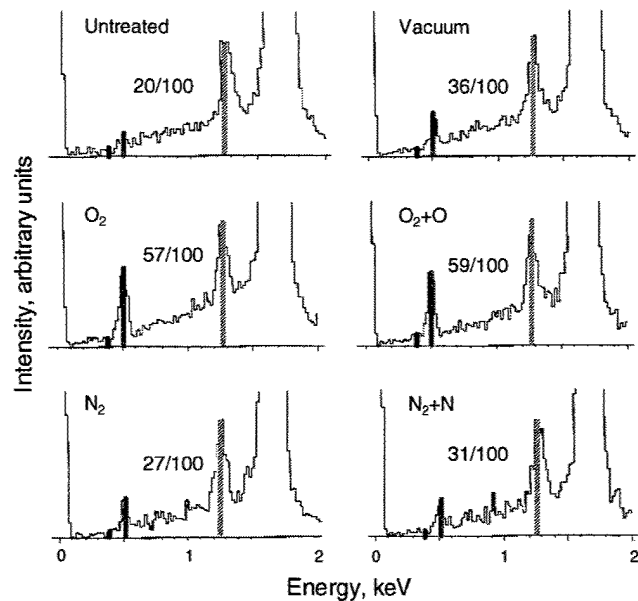
during the first run, a dramatic three orders of magnitude increase in the room temperature recombination coefficient, followed by a steady decrease in catalytic efficiency at 923 K to the quartz value during the second run. The third run again shows similar, though somewhat lower values, to the second run, and recombination coefficients are indistinguishable from quartz at 923 K.

Surface Analysis

Visually, no changes were observed in any of the specimens after run 1 heating cycles. After run 2 heating cycles, a faint tarnishing could be seen on the samples exposed to vacuum and nitrogen environments, whereas a more obvious discoloration was present on the samples exposed to oxygen environments. Similar results were seen for both the A-7 and A-8 specimens. These observations are consonant with the appearances of the catalysis test specimens after testing.

The run 2 A-7 specimens were examined by the use of EDX analysis. The results are summarized in Fig. 7. The N (0.392 keV), O (0.525 keV), and Hf (1.28 keV) peaks are indicated by black, gray, and banded bars, respectively. The nitrogen peak is negligibly small for all of the different test conditions. The EDX system is not sensitive to boron, and the silicon peaks at 1.74 and 1.836 keV are present but obscured by the strong hafnium peaks at 1.645 and 1.698 keV. The approximate ratio of the O to Hf peaks is also indicated in each panel. This ratio is about 0.20 in the untreated specimen, about one and one-half times larger for the vacuum and nitrogen exposed samples, and about three times larger for the oxygen exposed samples. There are no significant differences between the discharge-on and discharge-off spectra.

Figure 8 shows XPS survey spectra for the untreated A-7 sample, along with the A-7 samples exposed to oxygen and nitrogen during discharge-on run 1 and run 2 heating cycles. The oxygen, hafnium, and carbon peaks are prominent, whereas the silicon and boron peaks are very small. No nitrogen peak is seen. The surface composition of each sample (neglecting any contribution from silicon) was calculated with standard methods and published sensitivity factors.[20] Figure 9 plots the relative surface composition for these samples. Compared to the untreated sample, the oxygen to hafnium ratio increases by approximately 35% during the O$_2$ + O run 1 treatment, but then decreases to approximately 10% below the untreated sample during the O$_2$ + O run 2 treatment. Similarly, during the N$_2$ + N run 1 treatment, the oxygen to hafnium ratio increases by approximately 35% compared to the untreated sample and decreases to
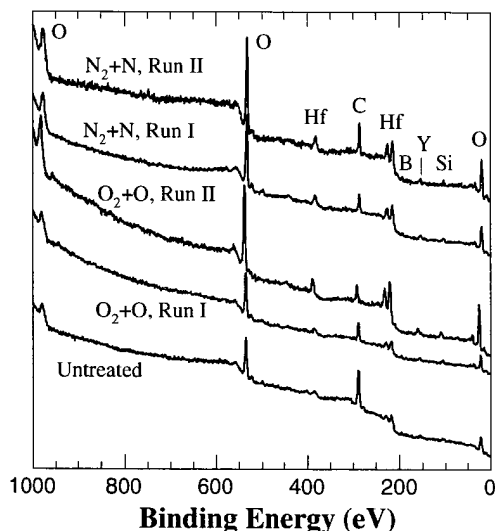
Fig. 8 XPS survey scans of A-7 (HfB_2, 20-vol% SiC) specimens exposed the oxygen and nitrogen with the discharge on; spectra have been offset to enable comparison.
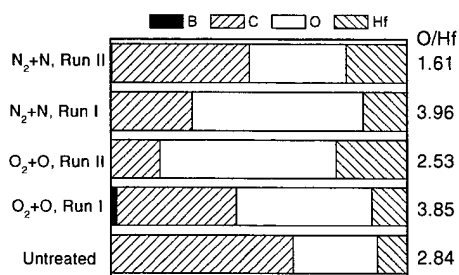

Fig. 9 XPS determined relative surface composition of the untreated, run 1, and run 2 A-7 samples exposed to oxygen and nitrogen with the discharge on.

approximately 40% below the untreated sample during the $N_2 + N$ run 2 treatment.

Discussion

The maximum oxygen and nitrogen recombination coefficients, measured at 473 and 673 K before samples are heated to 923 K, are about 5×10^{-2}. A recombination coefficient of 5×10^{-2} is similar to values measured in this same temperature range for oxidized Inconel 617, but is one to two orders of magnitude greater than typical values found for glassy silica-based coatings such as the reaction cured glass (RCG) shuttle tile coating.[21] When samples are heated to 923 K, catalytic efficiencies are seen to decrease steadily in time. Retesting of these samples reveals a lowered catalytic efficiency, in some cases indistinguishable from the quartz side-arm tube. This irreversible behavior suggests that some morphological and/or chemical changes are occurring at the sample surfaces during temperature cycling and gas exposure, even at these relatively mild environmental conditions.

Before suggesting possible scenarios for this behavior, we comment on the repeatability of the experimental technique and the accuracy of the derived recombination coefficients. For a chemically stable low catalytic efficiency material such as quartz, measurements made in rapid succession generally produce recombination coefficients that differ by less than 10%. Exceptions occur at high temperatures where the decreasing atom number density and the increasing thermal background from the furnace degrades the signal-to-noise ratio, or when initial heating or discharge operation produces transients associated with the removal of surface contaminates such as water. For materials with higher catalytic efficiency, the scatter in successive measurements is typically higher at a given temperature because more atoms are removed from the gas phase, lowering the LIF signal. However, this scatter still rarely exceeds

25%. It is evident that the systematic decreases in catalytic activity observed in successive measurements on UHTC samples heated to 923 K are not artifacts of experimental scatter. The observed changes are monotonic, large, and occurred on four different samples over the same temperature range.

The absolute accuracy of measured recombination coefficients is more problematic to evaluate. First, recombination coefficients extracted from the experimental data are coupled to the surface chemistry and gas flow assumptions used during data analysis. Because these vary with different techniques, it is safest to compare values for materials measured by the same experimental and data analysis approaches. Second, the recombination coefficient values we obtain are effective values in the sense that both the intrinsic material chemistry and the microscopic reactive surface area contribute to the measured value. We make no attempt to separate these contributions experimentally. Test samples are prepared as they would be for actual service; that is, we employ EDM and surface grinding techniques consistent with those used for the SHARP B1 and SHARP B2 flight articles. Third, when UHTC materials are tested it is likely that some recombination of atoms occurs on the ends and outer cylindrical surface of the tubular specimens, because the fit between the samples and the quartz tube inserts was not snug. Data were evaluated by the use of the inner diameter of the quartz tube inserts, which could lead to a systematic overestimation by a factor of $\sim$2. Thus, we make no claims of absolute accuracy beyond order-of-magnitude type quantification, which is sufficient to place the maximum observed UHTC catalytic efficiencies in the range typically seen for oxidized metals and from one to two orders of magnitude above the range for silica, quartz, and RCG.

We now present some possible scenarios for the transient catalytic behavior described earlier. For the oxygen-exposed samples, the results can be rationalized under the presumption of the formation of a B_2O_3 surface oxide. Crystalline B_2O_3 has a well-defined melting point of $\sim$723 K that lies above 673 K, the highest temperature that produced no irreversible changes in catalytic efficiency, and below 923 K, where steady declines in catalytic efficiency were observed. Amorphous B_2O_3 glass does not have a distinct melting point, but softening temperatures between $\sim$830 and 900 K have been reported.[22] The formation and melting of B_2O_3 could plausibly lead to lower catalytic efficiency, either by decreasing the reactive surface area as the B_2O_3 melts or because B_2O_3 is inherently less catalytic than the underlying UHTC material.

The temperature and oxygen partial pressure conditions present during catalysis testing should restrict any oxidation of SiC, ZrB_2, or HfB_2 to the passive oxidation regime where no volatile oxides are formed directly.[23,24] A very rough estimation of B_2O_3 oxide growth, based on the activation energy and pressure dependence of the ZrB_2 oxidation rate determined by Kuriakose and Margrave,[25] predicts $\sim$230 nm of B_2O_3 after 10 h of exposure to 923 K and 0.3 torr oxygen. The oxidation rate for SiC should be much slower, and similar estimates based on an extrapolation of the single-crystal SiC oxidation rates measured by Zheng et al.[26] predict a $\sim$3-nm-thick SiO_2 layer. Though dissociated oxygen can cause more rapid oxidation, this is not likely to be a significant mechanism in our experiments because the ratio of O atoms to O_2 molecules is less than $\sim$10^{-3} at the sample location in the side-arm reactor.

Support for surface oxidation under the catalysis test conditions is provided by the EDX measurements, which show a significant increase in the O/Hf ratio for the A-7 samples after exposure to oxygen and heating to 923 K. A similar increase is seen in the XPS result for the A-7 sample heated to 673 K in $O + O_2$, though the XPS results for the analogous sample heated to 923 K show a drop in this ratio. Some discrepancy between EDX and XPS trends are expected because XPS is very sensitive to surface contamination, such as adventitious hydrocarbons and surface depletion and/or enrichment of elements. EDX data are less affected by monolayer scale changes on the surface and will better reflect changes in the top micrometer or so of material.

For the nitrogen-exposed samples, the surface catalysis results are more puzzling. The initial decrease in catalytic efficiency suggests a transient period of surface reaction involving N atoms and

surface adsorbed species that tie up active sites on the surface. After the first heating cycle to 673 K, the second room temperature test reveals a much higher catalytic activity at room temperature, which is consistent with the thermal desorption of adsorbed species from the active sites, freeing them to be sites for N-atom recombination.

The irreversible reduction in catalytic efficiency at high temperature is difficult to explain in terms of nitrogen chemistry because nitride formation does not seem reasonable at these temperatures. Moreover, no nitrogen signatures were found in either the EDX or the XPS surface analysis. In principle, B_2O_3 should not form during these experiments, but in practice it is plausible that residual air leaks in the side-arm reactor system could admit sufficient oxygen into the test environment. The side-arm reactor is constructed of glassware joined by O-ring fittings and does not reach a base pressure below a few millitorr. EDX measurements support this view because both samples heated in a (nominal) vacuum and under nitrogen exhibit larger O/Hf ratios than the untreated specimen. If it is postulated that B_2O_3 is formed, then the reduction of the catalytic efficiency during the second run at 923 K could be ascribed to a similar B_2O_3 melting/coating phenomena as that for the oxygen catalysis experiments. This hypothesis is also consistent with the general reduction of catalytic efficiency during the third runs that occurred in the oxygen experiments.

In actual application, these materials are expected to see much higher surface temperatures and experience significant surface shear stresses. Boron oxide surface layers will not survive, both because shear forces will strip the B_2O_3 melt from leading edges and because B_2O_3 evaporation becomes significant above about 1500 K (Refs. 6, 27, and 28). However, a similar interplay between surface oxidation and surface catalytic efficiency might be anticipated at higher temperatures were silica formation and subsequent melting become significant. This elevated temperature regime (above ~1500 K) cannot be accessed by the use of side-arm diffusion-tube techniques and awaits exploration with arc-jet testing.[17,29]

Conclusions

The two major findings of this study are as follows:

1) The efficiency of ZrB_2/SiC and HfB_2/SiC composites for recombining dissociated oxygen and nitrogen can be nonnegligible between room temperature and 1000 K, with maximum observed recombination coefficients of ~5×10^{-2}.

2) The catalytic efficiency of UHTC materials can be altered by interactions with the environment even at relatively low temperatures; in particular, surface oxidation appears to lower the catalytic efficiency below that of the virgin material.

For aeroconvective heating computations, we suggest that, for temperatures up to 1000 K, a constant (temperature-independent) recombination coefficient of 0.1 would be an appropriate compromise between the extreme conservative limit of 1 and the observed maximum of 5×10^{-2}. Above 1000 K, it would be advisable to use the limiting value of 1 until the true situation is explored experimentally.

Acknowledgments

References

[1]Upadhya, K., Yang, J.-M., and Hoffman, W. P., "Materials for Ultrahigh Temperature Structural Applications," *American Ceramic Society Bulletin*, Vol. 76, No. 12, 1997, pp. 51–56.

[2]Kaufman, L., "Boride Composites—A New Generation of Nose Cap and Leading Edge Materials for Reusable Lifting Re-Entry Systems," AIAA Paper 70-278, Feb. 1970.

[3]Clougherty, E. V., Pober, R. L., and Kaufman, L., "Synthesis of Oxidation Resistant Metal Diboride Composites," *Transactions of the Metallurgical Society of AIME*, Vol. 242, June 1968, pp. 1077–1082.

[4]Tripp, W. C., Davis, H. H., and Graham, H. C., "Effect of an SiC Addition on the Oxidation of ZrB_2," *Ceramic Bulletin*, Vol. 52, No. 8, 1973, pp. 612–616.

[5]Bull, J., "The Influence of SiC on the Ablation Response of Advanced Refractory Composite Materials," *19th Conference on Composite Materials and Structures*, Pt. 1, Advanced Materials Processes and Technology Information Analysis Center, Rome, NY, 1995, pp. 157–181.

[6]Metcalfe, A. G., Elsner, N. B., Allen, D. T., Wuchina, E., Opeka, M., and Opila, E., "Oxidation of Hafnium Diboride," *Electrochemical Society Proceedings*, Vol. 99-38, 1999, pp. 489–501.

[7]Talmy, I. G., Zaykoski, J. A., and Opeka, M. A., "Properties of Ceramics in the ZrB_2/ZrC/SiC System Prepared by Reactive Processing," *Ceramic Engineering and Science Proceedings*, Vol. 19, No. 3, 1998, pp. 104–112.

[8]Bull, J., Kolodziej, P., Salute, J., and Keese, D., "Design, Instrumentation and Preflight Testing of a Sharp Ultra-High Temperature Ceramic Nosetip," NASA TM-1998-112229, Oct. 1998.

[9]Kolodziej, P., Bull, J., Salute, J., and Keese, D. L., "First Flight Demonstration of a Sharp Ultra-High Temperature Ceramic Nosetip," NASA TM-112215, Dec. 1997.

[10]Rakich, J. V., Stewart, D. A., and Lanfranco, M. J., "Results of a Flight Experiment on the Catalytic Efficiency of the Space Shuttle Heat Shield," AIAA Paper 82-0944, June 1982.

[11]Stewart, D. A., Rakich, J. V., and Lanfranco, M. J., "Catalytic Surface Effects on Space Shuttle Thermal Protection System During Earth Entry of Flights STS-2 Through STS-5," NASA CP-2283, March 1983.

[12]Stewart, D. A., Rakich, J. V., and Chen, Y.-K., "Flight Experiment Demonstrating the Effect of Surface Catalysis on the Heating Distribution Over the Space Shuttle Heat Shield," NASA CP-3248, April 1995.

[13]Linnett, J. W., and Rahman, M. L., "Recombination of Atoms at Surfaces, Part 13—Oxygen Atoms on $Zn_xFe_{3-x}O_4$ and $Ni_xFe_{3-x}O_4$," *Transactions of the Faraday Society*, Vol. 67, 1971, pp. 191–197.

[14]Cauquot, P., Cavadias, S., and Amouroux, J., "Thermal Energy Accommodation from Oxygen Atoms Recombination on Metallic Surfaces," *Journal of Thermophysics and Heat Transfer*, Vol. 12, No. 2, 1998, pp. 206–213.

[15]Marschall, J., "Experimental Determination of Oxygen and Nitrogen Recombination Coefficients at Elevated Temperature Using Laser-Induced Fluorescence," AIAA Paper 97-3879, Aug. 1997.

[16]Sepka, S., Chen, Y.-K., Marschall, J., and Copeland, R. A., "Experimental Investigation of Surface Reactions in Carbon Monoxide and Oxygen Mixtures," *Journal of Thermophysics and Heat Transfer*, Vol. 14, No. 1, 2000, pp. 45–52.

[17]Stewart, D. A., "Determination of Surface Catalytic Efficiency for Thermal Protection Materials—Room Temperature to Their Upper Use Limit," AIAA Paper 96-1863, June 1996.

[18]Smith, W. V., "The Surface Recombination of H Atoms and OH Radicals," *Journal of Chemical Physics*, Vol. 11, March 1943, pp. 110–125.

[19]Wood, B. J., and Wise, H., "The Interaction of Atoms with Solid Surfaces," *Rarefied Gas Dynamics*, edited by L. Talbot, Academic Press, New York, 1961, pp. 51–59.

[20]Briggs, D., and Seah, M. P. (eds.) *Practical Surface Analysis by Auger and X-Ray Photoelectron Spectroscopy*, Wiley, New York, 1983, pp. 181–214.

[21]Stewart, D. A., "Surface Catalysis and Characterization of Proposed Candidate TPS for Access-to-Space Vehicles," NASA TM-112206, July 1997.

[22]Rizzo, H. F., "Oxidation of Boron at Temperatures Between 400 and 1300°C in Air," *Boron-Synthesis, Structure, and Properties*, edited by J. A. Kohn and W. F. Nye, Plenum, New York, 1968, pp. 175–189.

[23]Vaughn, W. L., and Maahs, H. G., "Active-to-Passive Transition in the Oxidation of Silicon Carbide and Silicon Nitride in Air," *Journal of the American Ceramic Society*, Vol. 73, No. 6, 1990, pp. 1540–1543.

[24]Nixon, T. D., and Cawley, J. D., "Oxidation Inhibition Mechanism in Coated Carbon–Carbon Composites," *Journal of the American Ceramic Society*, Vol. 75, No. 3, 1992, pp. 703–708.

[25]Kuriakose, A. K., and Margrave, J. L., "The Oxidation Kinetics of Zirconium Diboride and Zirconium Carbide at High Temperatures," *Journal of the Electrochemical Society*, Vol. 111, No. 7, 1964, pp. 827–831.

[26]Zheng, Z., Tressler, R. E., and Spear, K. E., "Oxidation of Single-Crystal Silicon Carbide," *Journal of the Electrochemical Society*, Vol. 137, No. 3, 1990, pp. 854–858.

[27]Singh, M., and Wiedemeier, H., "Chemical Interactions in Diboride-Reinforced Oxide-Matrix Composites," *Journal of the American Ceramic Society*, Vol. 74, No. 4, 1991, pp. 724–727.

[28]Tripp, W. C., and Graham, H. C., "Thermogravimetric Study of the Oxidation of ZrB_2 in the Temperature Range of 800 to 1500°C," *Journal of the Electrochemical Society*, Vol. 118, No. 7, 1971, pp. 1195–1199.

[29]Stewart, D. A., Chen, Y.-K., Bamford, D. J., and Romanovsky, A. B., "Predicting Material Surface Catalytic Efficiency Using Arc-Jet Tests," AIAA Paper 95-2013, June 1995.

B. Hassan
Associate Editor

MODELING SURFACE OXIDATION IN TRANSIENT AEROTHERMAL HEATING ENVIRONMENTS

Jochen Marschall*
SRI International
Menlo Park, CA 94025

Y.-K. Chen[†]
NASA Ames Research Center
Moffett Field, CA 94035-1000

Abstract

This paper presents a computational model for simulating oxidation during transient aerothermal heating. The methodology and approach are discussed, and computational examples given for SiC oxidation. Results and avenues for further model development are discussed.

Nomenclature

Variables

a,b,c,d	stoichiometric coefficients, Eq. 1
B'	dimensionless mass flux
C_{int}	oxygen concentration at the oxide-substrate interface, moles m^{-3}
C_H	Stanton number for heat transfer
C_M	Stanton number for mass transfer
C_o	oxygen concentration in the oxide at the surface, moles m^{-3}
D	oxygen diffusion coefficient in oxide scale, m^2 s^{-1}
E_b	Planck's function, W m^{-3}
$E_{p,s}$	electric field vectors
H	Henry's constant for oxygen solubility in the oxide scale, moles m^{-3} Pa^{-1}
J	species flux, moles m^{-2} s^{-1}
k	imaginary part of refractive index
k_{ox}	oxidation rate constant, m/s
L	oxide layer thickness, m
m	complex refractive index
M	molar mass, kg mole^{-1}
n	real part of refractive index

Symbols

P	product
P_{O_2}	oxygen partial pressure, Pa
R	reactant, reflectivity, or universal gas constant, J mole^{-1} K^{-1}
t	time, s
T	temperature, K
u	velocity, m s^{-1}
Δ	oxide layer thickness, m
ε	emittance
λ	wavelength, m
ρ	density, kg m^{-3}

Subscripts

e	boundary layer edge
j,k,l	species indices, Eq. (1)
$scale$	oxide scale
sub	substrate
w	wall

Superscripts

i	time step index, Eqs. 4 and 5
g	gas
s	solid

* Research Scientist, Molecular Physics Laboratory, jochen.marschall@sri.com. Senior member AIAA.
† Aerospace Engineer, Thermal Protection Materials and Systems Branch, ykchen@mail.nasa.gov.

Introduction

High temperature oxidation is a ubiquitous issue for leading edge materials on hypersonic flight vehicles. A great deal of effort is spent trying to avoid or minimize its occurrence and to detect its presence on flight articles. Oxidation has long-term ramifications for reusability and service lifetime, and potentially catastrophic consequences when it compromises the integrity of crucial leading edge components.

Over the last decade there has been a renewed interest in ultra high temperature ceramic (UHTC) composites based on ZrB$_2$ and HfB$_2$ for use as sharp leading edge components on

hypersonic flight vehicles. Both the diborides and their primary metal oxides have extremely high melting points[1] and UHTC composites have shown good dimensional stability in low-pressure supersonic aerothermal heating environments, where other refractory materials rapidly fail by melting, spalling, pyrolyzing or ablating.[2]

However oxidation remains an important issue. Pure ZrB_2 and HfB_2 specimens do not exhibit good long-term oxidation resistance in high temperature oxidizing environments. At ZrO_2 and HfO_2 scales are not effective oxygen diffusion barriers and do not provide sufficient protection to the underlying virgin material to prevent unacceptable levels of internal oxidation. Several studies have demonstrated that the oxidation resistance of diboride-based composites is substantially enhanced by the addition of SiC.[3-6] The passive oxidation of SiC forms SiO_2, which is an effective oxygen diffusion barrier. At higher temperatures, the SiO_2 melts and coats the diboride oxide phases to form a protective scale. Cross-sections of furnace and arc-jet oxidized ZrB_2/SiC and HfB_2/SiC specimens reveal complicated multi-layer oxide structures, whose characteristics are dependent on the test environment.

Oxidation is a dynamic process, sensitive to perturbations in temperature and oxidant concentration. It is coupled to the flow environment both chemically and thermally. For the interpretation of transient test results, as produced for example by arc-jet exposure, and for the prediction of oxide formation during different flight conditions, a computational model of oxide formation in an aerothermal heating environment is desirable.

Here we report our initial efforts to develop a thermal response code that incorporates material loss and gain by surface oxidation. Our end goal is to develop a sufficiently sophisticated oxidation and thermal response program to model UHTC leading edge components.

Our approach is to begin by developing some of the necessary components for such a program, starting with a simpler one-dimensional geometry, a less-complicated material system, and equilibrium instead of finite rate chemistry calculations. The code we present here is designed to track the dynamic formation of oxide layers on simple silica formers (e.g., Si, SiC) during exposure to transient oxidizing aerothermal heating environments. Computational examples are given.

Overview

A useful numerical model for in-flight oxidation must strike a compromise between physical detail and computational efficacy. Before describing our numerical approach, we outline some of the relevant physics and modeling issues.

Active and Passive Oxidation

Oxidation involves the reaction of oxygen bearing species in the boundary layer with constituents in the substrate. Oxidation is "active" when only gaseous products are generated and "passive" when a stable, self-limiting oxide layer is formed. Active oxidation removes mass from the surface and provides no protection to the substrate, while passive oxidation incorporates oxygen into the surface to form a protective surface layer.

Computationally, the rate of material removal during active oxidation can be modeled using chemical equilibrium or finite rate chemistry. Passive oxidation requires a model of gas diffusion and internal reaction to compute the rate that substrate material is consumed and oxide grown. Either internal gas transport rates or internal reaction rates can be the limiting mechanism for passive oxidation.

The details of the oxidation process become increasingly complicated as the materials involved become more complex. As the number of constituents increase, the number of possible reactions, and solid and gaseous products, multiply. Experimentally, it is observed that oxide scales can form multi-layer structures, wherein the composition and morphology of each layer differs. Modeling such systems entails tracking gaseous fluxes into and out of each layer, with an attendant set of gas-gas and gas-surface reactions for each layer or interface between layers.

Flow Field

Both active and passive oxidation can be limited by the availability of oxide bearing species in the boundary layer. Even under nominal steady-state conditions, as in furnace oxidation studies, gas flow conditions can alter observed oxidation rates and determine the transition between active and passive oxidation. Under supersonic flow conditions, the transport of reactants to and products from oxidizing surfaces is clearly coupled to the flow environment. The concentration of oxide bearing species at the surface depends on the chemical composition and

the structure of the surrounding flow field, and must be computed using computational fluid dynamics with either equilibrium or finite rate chemistry approaches.

Surface Properties

The thermal and chemical characteristics of oxidized and virgin surfaces can differ substantially. The emittance of a surface can change through oxidation, altering a material's ability to reject heat via radiation. This changes the temperatures attained by a component under aerothermal heating and also interferes with surface temperature measurements based on detection of emitted radiation.

A portion of the aerothermal heating experienced during hypervelocity flight can be attributed to the dissociation of molecular species in the bow shock and the subsequent recombination of these species on the surface. Oxidation can alter the catalytic efficiency of a surface for recombining dissociated species, as recently demonstrated for ZrB_2/SiC and HfB_2/SiC.[7]

Bulk Properties

As oxides layers form and grow, their bulk properties begin to influence the mechanical stability and thermal response of the component. The density, thermal expansion coefficient, elastic modulus, heat capacity and thermal conductivity will all change from that of the virgin substrate.

Changes in the thermal conductivity can be significant. For example, at 1200 K the thermal conductivity of SiO_2 is only about 1/15 of that for SiC.[8] Similar large thermal conductivity differences exist between ZrB_2 and ZrO_2, and HfB_2 and HfO_2.

In addition, microstructural changes, such as pore formation and cracking, can occur in the oxide or at the oxide-substrate interface leading to the detachment. Poor physical contact between the oxide and the substrate decreases heat conduction into the substrate and leads to higher surface temperatures on the oxide surface for the same heat input. The mechanical failure of a protective oxide layer will also expose virgin surface directly and abruptly to the environment.

Computational Formulation

We have modified the one-dimensional thermal response program FIAT to include the formation of a surface oxide layer, use the ACE thermochemistry program to calculate chemical equilibrium gas compositions, and apply this approach to simulate the oxidation SiC surfaces.

Thermal Response Model

The FIAT program was developed at NASA Ames Research Center for computing one-dimensional energy transport in multilayer thermal protection systems that can ablate from the surface and decompose in depth[9]. FIAT uses finite volume descretization and an implicit numerical scheme to solve surface energy balance, internal energy balance, internal decomposition and internal mass balance equations at each time step. The program accepts convective heat transfer boundary conditions specified in terms of heat transfer coefficients and recovery enthalpy at the wall, as usually employed for aerothermal heating simulations.

FIAT is more stable than the well-known CMA program[10], which solves essentially the same equations. FIAT also provides interfaces with the flow codes GIANTS and GASP, and the thermochemistry codes ACE and MAT, for high fidelity, thermal response computations strongly-coupled to the flow field.

At each time step, for a given surface temperature and oxygen partial pressure at the wall, the modified FIAT program evaluates whether conditions favor passive or active oxidation. For the present work we use the transition boundary presented by Balat et al.[11], in their study of active and passive oxidation of silicon carbide. This boundary is shown in Fig. 1 along with experimentally derived passive-to-active transition points. The scatter in experimental values is considerable and can be attributed to differences in experimental technique and SiC material. The transition line of Balat et al. is conservative in the sense that it places almost all experimental data in the active oxidation field.
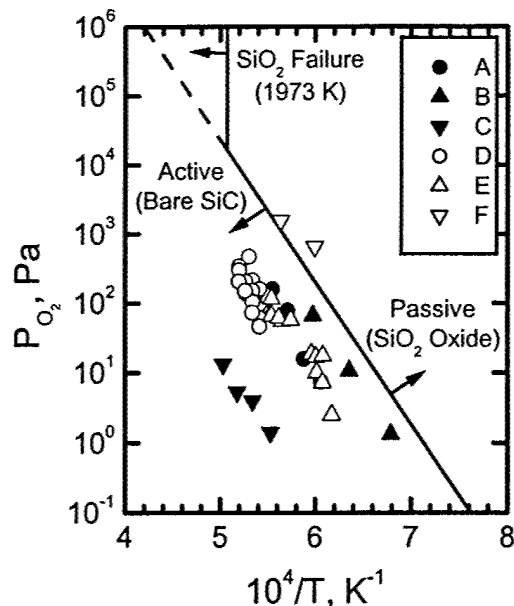
Figure 1. Active and passive oxidation regimes of SiC. Experimental data: A[12]; B[13]; C[14]; D[15]; E[16]; F[11]. Active-passive transition line adapted from Balat et al[11].
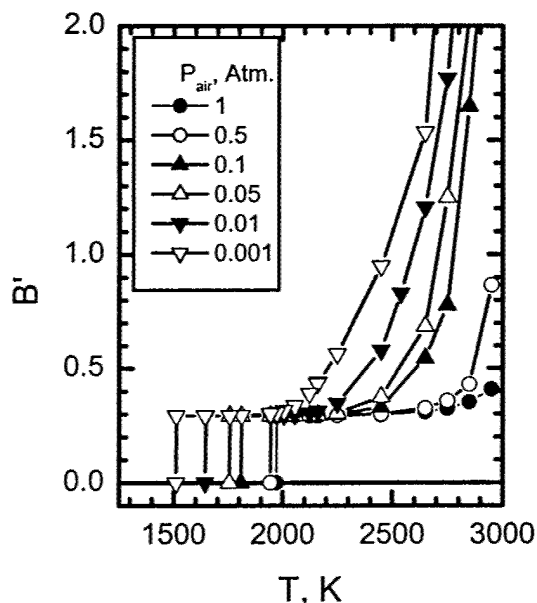

Figure 2. B' as a function of temperatutre and pressure for a bare silicon carbide surface in air.

When surface temperature and pressure conditions place the surface in the active oxidation regime, the surface is taken as bare SiC and mass

loss is computed using B' tables generated by ACE. B' is a dimensionless mass flux defined by $\dot{m} / \rho_e u_e C_M$, where C_M is the Stanton number for mass transfer.

ACE is a thermochemistry code that computes the equilibrium (or non-equilibrium) steady-state chemistry between a surface and its gas environment[17]. This calculation is coupled with a surface mass balance that accounts for material leaving the surface as pyrolysis gases, ablation products and thermomechanically failed material as well as for gaseous species diffusing in from the boundary layer edge. Usually, the convective transfer coefficients C_M and C_H are used to describe mass and heat transfer to the surface, respectively. In general these convective coefficients must be supplied by a CFD calculation as a function of flow environment, vehicle shape, trajectory, etc. Analytic correlations are also available and often the transfer coefficients are constrained by assuming a Lewis number of one (i.e., the equivalence of thermal and mass diffusivity through the boundary layer).

B' values are functions of temperature, pressure and gas composition. Figure 2 shows B' curves computed for SiC under different temperature and air pressure combinations.

If a SiO_2 layer exists on the SiC surface when conditions pass from passive to active, the oxide becomes unstable due to reactions between SiC and SiO_2 that produce volatile SiO gas. The actual dynamics of this process are uncertain. Presently, we model the transition as abrupt and remove the oxide layer completely.

Similarly, we model the melt failure of the SiO_2 oxide as an abrupt process at 1973 K. If the temperature rises above this value, existing oxide layers are completely removed and a bare SiC surface is imposed. No stable oxide is allowed to form above 1973 K, even in the nominally passive regime, rather all oxidation products contribute to mass loss.

When surface temperature and oxygen pressure conditions favor passive oxidation, oxide growth and substrate consumption are calculated and the layer thickness incremented at each time step. Surface properties like emittance are adjusted to reflect the current oxide thickness. For oxide layers thinner than the computational volume element, the influence of oxide thermal properties on thermal response are included by calculating effective values based on the relative amounts of oxide and substrate material in the

volume element. When the oxide thickness approaches the volume element thickness required for accurate thermal response computations, the oxide is given its own volume element.

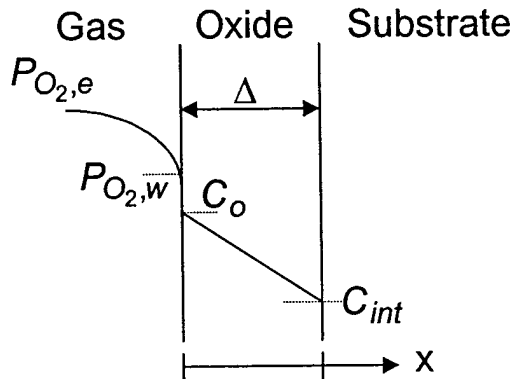The sub-sections below describe the dynamic oxide growth and emittance models.

Figure 3. Oxide growth schematic.

Oxide Growth Model

We develop a simple oxide growth model based on the principle that the rate of scale production is directly proportional to the rate that oxygen molecules are consumed by the relevant oxidation reaction at the oxide-substrate interface. The relevant geometry and physical parameters are illustrated in Fig. 3.

If the oxidation reaction is of the form

$$aO_2 + \sum_j b_j R_j^s = \sum_k c_k P_k^g + \sum_l d_l P_l^s , \qquad (1)$$

the rate of scale formation is

$$\frac{d\Delta_{scale}}{dt} = \sum_l J_{P_l^s} \frac{M_l}{\rho_l} = J_{O_2} \sum_l \frac{d_l}{a} \frac{M_l}{\rho_l} \qquad (2)$$

and the rate of substrate consumption is

$$\frac{d\Delta_{sub}}{dt} = -\sum_j J_{R_j^s} \frac{M_j}{\rho_j} = -J_{O_2} \sum_j \frac{b_j}{a} \frac{M_j}{\rho_j} . \qquad (3)$$

These two equations can be discretized for numerical calculation of the scale and substrate thickness as a function of time;

$$\Delta_{scale}^{i+1} = \Delta_{scale}^i + (t^{i+1} - t^i) J_{O_2}^i \sum_l \frac{d_l}{a} \frac{M_l}{\rho_l} \qquad (4)$$
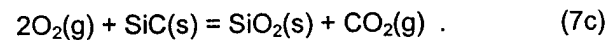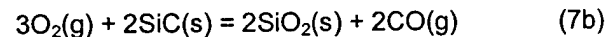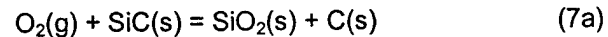
and

$$\Delta_{sub}^{i+1} = \Delta_{sub}^i - (t^{i+1} - t^i) J_{O_2}^i \sum_j \frac{b_j}{a} \frac{M_j}{\rho_{ji}} . \qquad (5)$$

For passive silicon oxidation the relevant reaction is

$$O_2 + Si(s) = SiO_2(s) \qquad (6)$$

giving $b_1/a = d_1/a = 1$. For passive SiC oxidation three different reactions are possible:

$$O_2(g) + SiC(s) = SiO_2(s) + C(s) \qquad (7a)$$

$$3O_2(g) + 2SiC(s) = 2SiO_2(s) + 2CO(g) \qquad (7b)$$

$$2O_2(g) + SiC(s) = SiO_2(s) + CO_2(g) . \qquad (7c)$$

Reaction (7a) gives $b_1/a = d_1/a = d_2/a = 1$, reaction (7b) gives $b_1/a = d_1/a = 2/3$, and reaction (7c) gives $b_1/a = d_1/a = 1/2$.

Under quasi-steady state conditions and assuming a constant diffusion coefficient, oxygen diffusion through the scale can be described by Fick's law

$$D \frac{d^2 C}{dx^2} = 0 \qquad (8)$$

with the boundary conditions

$$C(0) = C_o = H P_{O_2,w} \qquad (9a)$$

and

$$J_{O_2} = -D \frac{dC}{dx}\Bigg|_{\Delta_{scale}} = k_{ox} C_{int} . \qquad (9b)$$

Here the concentration of molecular oxygen just inside the scale is related to the molecular concentration in the gas at the surface by Henry's law and the oxidation reaction is assumed to be first order in oxygen concentration at the oxide-substrate interface.

The solution for oxygen concentration is

$$C(x) = HP_{O_2,w}\left[1 - \frac{k_{ox}x}{D + k_{ox}\Delta_{scale}}\right] \qquad (10)$$

and the general form for the flux of oxygen consumed at the oxide-substrate interface is

$$J_{O_2} = \frac{P_{O_2,w}Hk_{ox}D}{D + k_{ox}\Delta_{scale}} . \qquad (11)$$

When oxidation is limited by diffusion to the oxide-substrate interface, $C_{int} \to 0$, the oxygen flux reduces to $P_{O_2,w}HD/\Delta_{scale}$ and substitution into equation (2) results in a parabolic oxide growth law. When oxidation is limited by the reaction rate at the interface, $C_{int} \to C_o$, the flux reduces to $P_{O_2,w}Hk_{ox}$ and the oxide growth rate is linear.

This model essentially reproduces the classic Deal-Grove model[18] which captures most of the important physics involved in the oxidation of silica forming materials: the mass transport of oxygen to the oxide surface, the solubility of oxygen in the oxide adjacent to the gas, the diffusion of oxygen through the oxide layer to the substrate-oxide interface, and the reaction of oxygen with the substrate to form new oxide. However, we write the flux relation (11) in terms of $P_{O_2,w}$, and don't explicitly incorporate a mass transport coefficient relating the free-stream and surface oxygen concentrations, this transport coefficient being supplied in general by a CFD solution.

For the initial calculations we present here, we assume that the oxidation reaction at the interface is large enough to ensure that passive oxidation is limited by diffusion, resulting in parabolic kinetics. This assumption is consistent with the vast majority of experimental observations on silica formers, as summarized by Jacobson [19].

The temperature dependence of the parabolic oxide growth rate reflects the temperature dependence of the oxygen diffusion coefficient, while Henry's constant is approximately independent of temperature.[18] To calculate oxide growth, numerical values must be assigned to the product $HD_0 \exp[E/RT]$. We take $H = 8.5 \times 10^{-7}$ moles m^{-3} Pa^{-1}, a value consistent with the experiments of Norton[20] and Deal and Grove.[18] Many different choices exist in the literature for D_0 and E, these quantities being dependent upon microstructure, processing, impurities, etc. of the SiC sample.[19] For the present computations, we set D_0 and E by fitting the parabolic oxide growth rates presented by Costello and Tressler[21] for three different polycrystalline SiC samples oxidized in one atmosphere of dry oxygen over the 1200 C to 1500 C temperature range. This procedure gives

$$D = 8.5 \times 10^{-6} \exp\left[\frac{-193800}{RT}\right] . \qquad (12)$$

Emittance Variations

The dynamic emittance of an oxidizing surface is function of direction, wavelength, temperature, and oxide thickness and morphology. Ideally, emittance should be measured as a function of these parameters, but this is difficult to do.

The major changes in emittance associated with transient temperature variations and oxide layer growth are simulated by computing thin film optics solutions for the spectral directional reflectance and absorbance of a vacuum-oxide-substrate system, using Kirchhoff's law to obtain spectral directional emittance from absorbance, and finally computing the temperature-dependent total hemispherical emittance by averaging over all directions and the Planck function.

Analytic expressions for the spectral, directional reflectance of an absorbing film, sandwiched between semi-infinite transparent and absorbing layers, have been given by Heavens[22] for normal incidence and Abelès[23] for oblique incidence. The reflectance is an explicit function of the complex refractive indices of the three layers, and the wavelength, polarization and incident angle of the impinging light. A FORTRAN program was written based on Abelès's (corrected) expressions; see Appendix 1. Program outputs were compared to various published test cases and excellent agreement was confirmed.

The reflectance for unpolarized light is the average of the reflectance calculated for s- and p-polarized light. The spectral, directional absorbance of an opaque material is one minus its spectral, directional reflectance. According to Kirchhoff's law, the spectral, directional emittance is equal to the spectral, directional absorbance. Thus the thin film optics calculations lead directly to the spectral, directional emittance as a function of oxide layer thickness.

The room temperature complex refractive indices of SiC and SiO$_2$ glass over the 0.05 to 25 μm wavelength range were taken from Palik[24].

The spectral, hemispherical emittance was calculated by integrating the spectral directional emittance; viz.,

$$\varepsilon(298,\lambda) = 2 \int_0^{\pi/2} \varepsilon(298,\lambda,\theta)\cos\theta \sin\theta \, d\theta \ , \qquad (13)$$

assuming an isotropic surface (no dependence on azimuthal angle.) The integral in Equation 13 was evaluated numerically using a simple trapezoidal integration routine and directional emittance values calculated at five degree intervals.

The total hemispherical emittance at a fixed temperature was then calculated by averaging the room-temperature spectral hemispherical emittance over the Planck function,

$$\varepsilon(T) \cong \frac{\int_{\lambda_1}^{\lambda_2} \varepsilon(298,\lambda)E_b(T,\lambda)\,d\lambda}{\int_{\lambda_1}^{\lambda_2} E_b(T,\lambda)\,d\lambda} \qquad (14)$$

where λ_1 and λ_2 bound the wavelength interval of available refractive index data.

This integration procedure assumes that the emittance temperature dependence is dominated by Planck's function, not by the temperature dependence of the complex refractive indices of the materials, a reasonable assumption given the lack of accurate high temperature optical constant data and the general consensus that total (i.e., spectrally averaged) quantities are not very sensitive to small temperature-induced variations in the spectral optical constants. For example, Tropf and Thomas [25] have calculated a difference of less than 1% when room temperature rather than elevated temperature optical constants were used to evaluate the hemispherical emittance of SiO_2 at 1300 K.

The wavelength range 0.05 to 25 microns includes about 83.4%, 99.2%, and 99.9% of total power radiated by a blackbody at 300 K, 1000 K and 2000 K, respectively. Equation (14) was evaluated with a trapezoidal scheme using 1000 wavelength intervals spaced to maximize resolution of the emissive power. The spectral emissive power of a blackbody is a strong non-linear function of temperature and wavelength. Therefore, the integration intervals were chosen such that the emissive power was approximately equal in each wavelength increment. This procedure ensures that the integrand in the numerator of equation (14) is highly resolved in wavelength regions where the emissive power is strongest at each temperature.
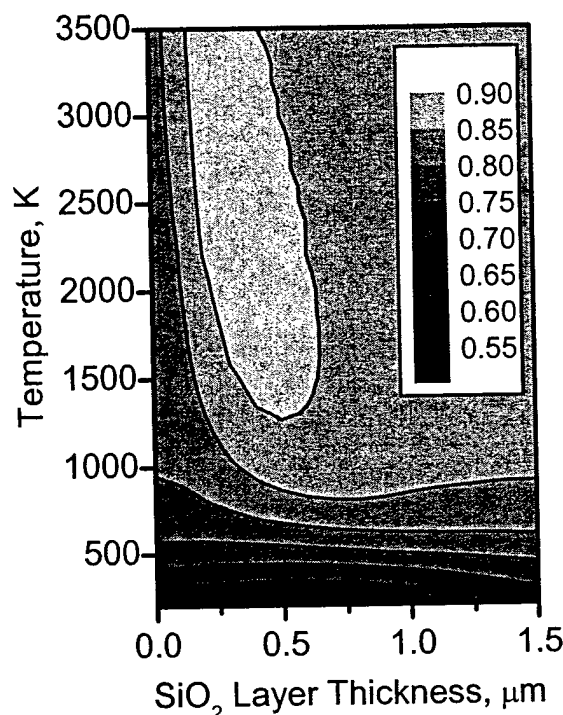

Figure 4. The computed total hemispherical emittance of a SiC surface, as a function of temperature and SiO_2 thickness.

Computational Example

As a computational example we present a simple simulation of SiC oxidation under transient heating and pressure conditions representative of an atmospheric entry. We make rough approximations – see Fig. 5 - to the atmospheric entry conditions for the HL-20 crew transfer vehicle trajectory, as presented by Saunders et al. [26]. From these approximations we estimate the heat transfer coefficient and recovery enthalpy at 0, 500, 1500, and 2100 seconds, and then use linear interpolations of these quantities as transient thermal boundary conditions. We scale (by 0.23) linear interpolations of the dynamic pressure to set transient O_2 partial pressures at the wall.
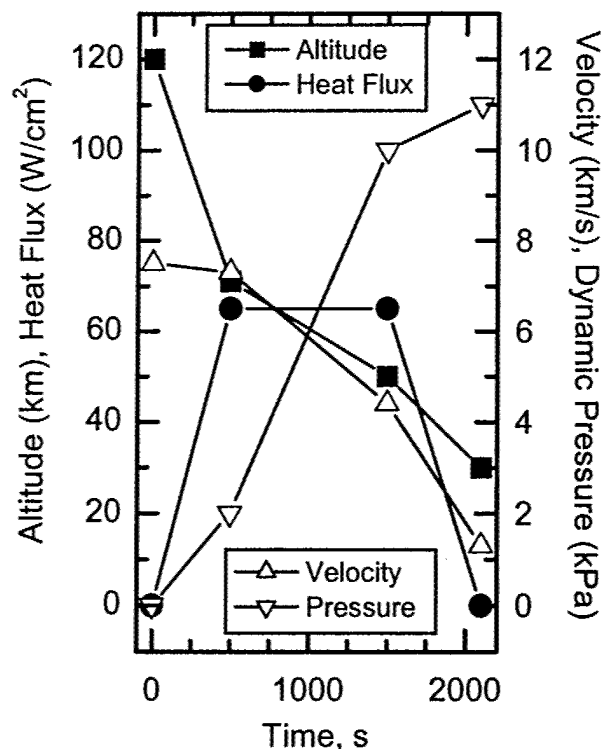
Figure 5. Rough approximations to the HL-20 entry conditions presented by Saunders et al. [26].
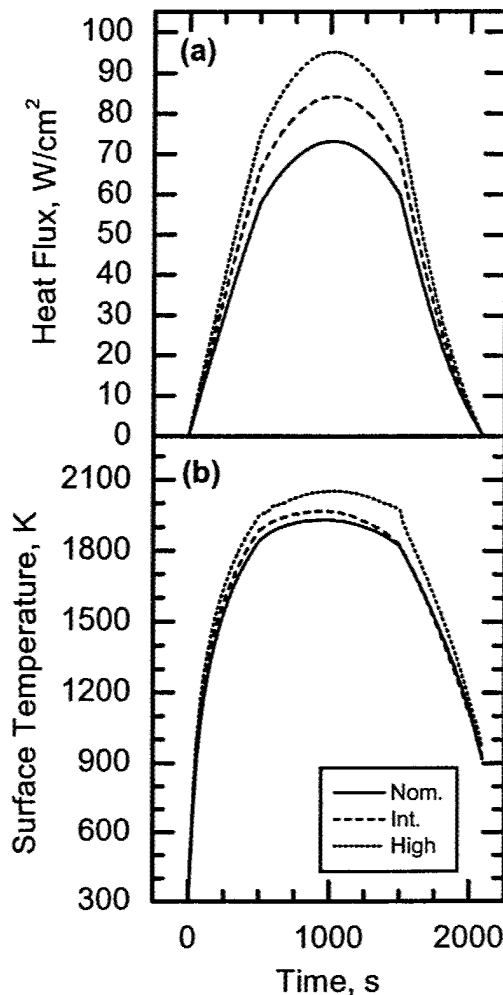

Figure 6. (a) heat flux and (b) resulting surface temperature for an initially bare SiC sample exposed to three different transient heating environments.

Calculations are made for a 1 inch thick slab of initially bare SiC, with an adiabatic back wall and an initial temperature of 300 K. A Lewis number of one is assumed. Three different heating levels are considered: nominal, intermediate (scaled by 1.15), and high (scaled by 1.30.)

The computational results for this example are shown in Figs. 6 and 7. In all cases the temperature-pressure regime is such that passive oxidation is favored over active oxidation. For the nominal and intermediate cases, the surface temperature remains below the assigned SiO_2 fail temperature of 1973 K, and SiO_2 growth is computed through out the heat pulse. Oxide layers between 300 and 400 nm thick are predicted, with more oxide growth in the intermediate than the nominal heat flux case, owing to more efficient oxygen diffusion through the scale at higher temperatures.

In the high heat flux case, surface temperatures rise above the SiO_2 fail temperature and the surface reverts back to bare SiC. With loss of the protective silica, SiC mass loss is dramatically accelerated and the cumulative consumption of SiC at the end of the heat pulse in the range of millimeters. After peak heating, the surface temperature drops below the fail temperature and SiO_2 growth resumes.
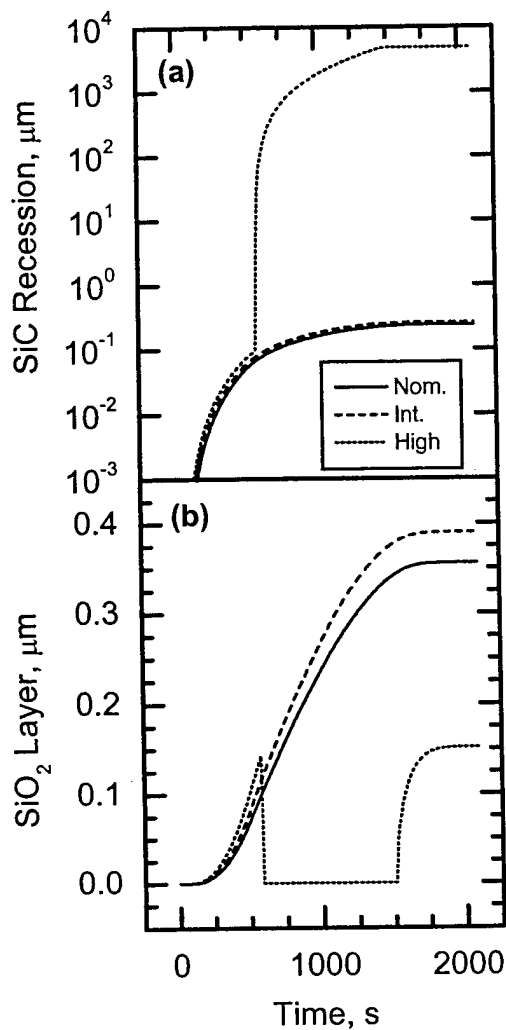
Figure 7. (a) SiC recession and (b) SiO₂ growth for the three different transient heating environments shown in Fig. 6 (a).

Figure 8. Total hemispherical emittance as a function of time.

Changes in the hemispherical emittance over time are shown in Fig. 8. The initial sharp rise in emittance is mostly due to the rapid increase in surface temperature as the heating rate ramps up. Further increases in emittance, for the nominal and intermediate cases, result as SiO₂ layers grow, while the plateau seen for the high heat flux case reflects the bare SiC surface above the SiO₂ fail temperature.

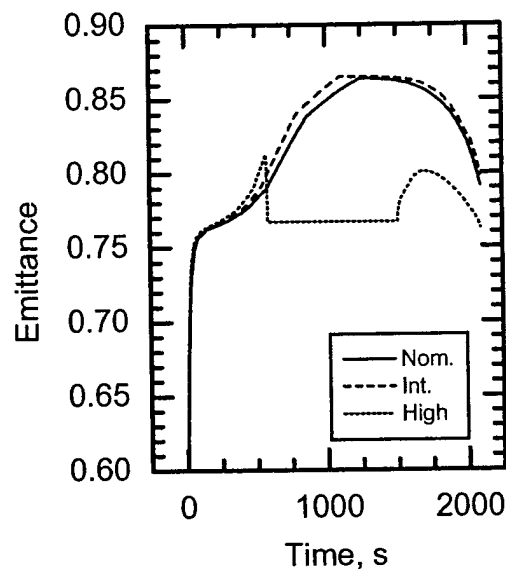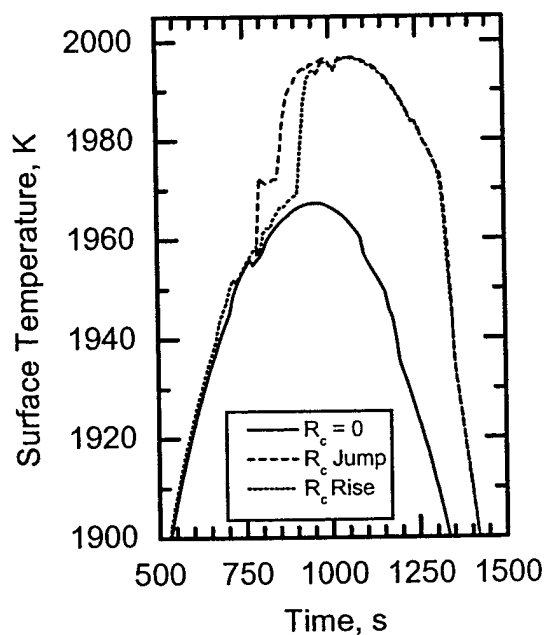Figure 9. The effect of increasing contact resistance on surface temperature.
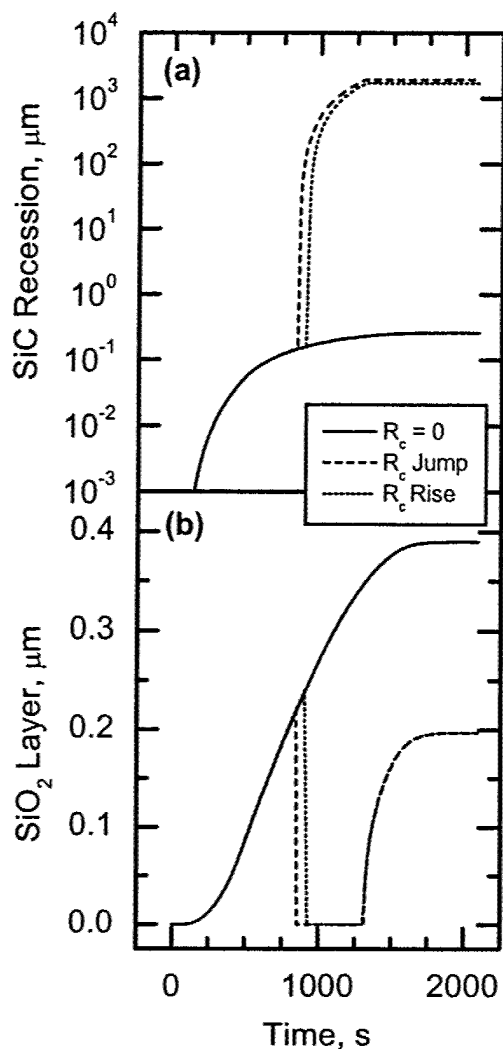
Figure 10. Failure of oxide layer due to increasing contact resistance; (a) SiC recession and (b) SiO_2 layer thickness.

Adhesion between the oxide scale and the substrate is important for stability and reusability. If an appreciable contact resistance develops between the oxide and the substrate, the temperature in the oxide scale can rise and may exceed the oxide melting point. This phenomenon can be simulated by changing the contact resistance between the oxide and substrate according to some function of temperature, stress, oxide thickness, etc.

We consider two illustrative cases in which the contact resistance varies with oxide layer thickness. The first is a sudden, 100-fold jump in the thermal resistance between oxide and substrate when the oxide thickness exceeds 200 nm. This case simulates the sudden loss of scale adhesion. The second case is a monotonic, quadratic increase in thermal resistance with oxide layer thickness, reaching 400-fold increase at 200 nm scale thickness. This case simulates a steady increase in thermal resistance as produced, for example, by the development of a porous interlayer near the scale-substrate interface.

Figure 9 shows the resulting temperature jumps using the intermediate heating profile. The corresponding SiO_2 thickness and SiC recession plots are shown in Fig. 10.

Discussion

The computational examples demonstrate that the modified version of FIAT can model oxide growth and substrate recession during transient heating and pressure profiles, and can incorporate oxide dependent optical and thermal properties into the thermal response analysis.

In principle, the model could be "tuned" to match experimental oxidation results for a particular SiC materials subjected to various aerothermal heating environments, much as is done for ablators.

Various model enhancements can be made by relatively straightforward coding additions. For example, currently a single fail temperature is used for all oxide failure modes (melting, mechanical failure.) A separate criteria for mechanical failure in the passive regime below the melting temperature, would allow removal of the oxide layer followed by oxide re-growth (i.e., oxide "healing".) The code could also be modified to allow for pre-existing oxide layers, enabling "multi-use" simulations.

With more effort, the basic oxide growth model can be extended to multi constituent, multi-layer oxides. More complication is added by the additional reactions, layer interfaces and diffusion relations, but analytic models exist in the literature that can be adapted [27-30], and the addition of this capability will be necessary for the ultimate goal of simulating UHTC oxide formation.

More serious barriers to further model development are the limitations imposed by the chemical equilibrium solutions for an open system, as solved by the ACE program. In principle, the boundary between the active and passive oxidation regimes should be determined from equilibrium thermochemical calculations, however

ACE is not able to reproduce the observed active to passive transition for an open O_2/SiC system.

For a closed system, given the mass fractions and elemental compositions of the reactants, the pressure, and the temperature, ACE can compute the partial pressures of all candidate gas species, the mass fractions of all candidate condensed species, and the system molar mass. For a closed O_2/SiC system, ACE can provide satisfactory solutions that shift from active (SiC condensed species) to passive (SiO_2 condensed species) oxidation conditions as a function of the O_2/SiC mass ratio.

For an open system, given the elemental compositions of the reactants, dimensionless mass transfer rates, and pressure, ACE can compute the partial pressures of all candidate gas species, the elemental mass fractions at the wall, the system molar mass, and the temperature. ACE chooses only one species from the list of candidate condensed species and includes only the equilibrium formation reaction for this condensed species in the equation set.

For the O_2/SiC system, ACE chooses SiO_2 as the surface species for all B' values below 1.25, the mass flux ratio that exactly satisfies the active oxidation reaction:

$$O_2(g) + SiC(s) = SiO(g) + CO(g) \ . \qquad (15)$$
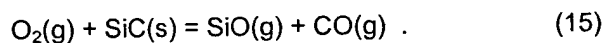
(For air this same transition occurs at $B' = 0.29$.)

Above $B' = 1.25$, ACE chooses SiC as the condensed species, and the B' curves are single valued functions of temperature, that can be used to model active SiC oxidation. However, below $B' = 1.25$, ACE produces B' curves that are double valued functions of temperature over a significant B' range. Moreover, the temperatures in this range are often above the silica melting point.

As an example, the B' curve calculated by ACE for an oxygen pressure of 101 Pa is presented in Fig. 11. Experimentally, the transition from passive to active SiC oxidation should occur between ~ 1750 and 2000 K; see Fig. 1. The program does not predict such a transition as the temperature is raised through this range. The only way to reproduce the experimental active-passive transition data is to assign a suitable SiO_2 fail temperature at each pressure, forcing the transition to condensed SiC. This was done to generate the B' curves of Fig. 2.
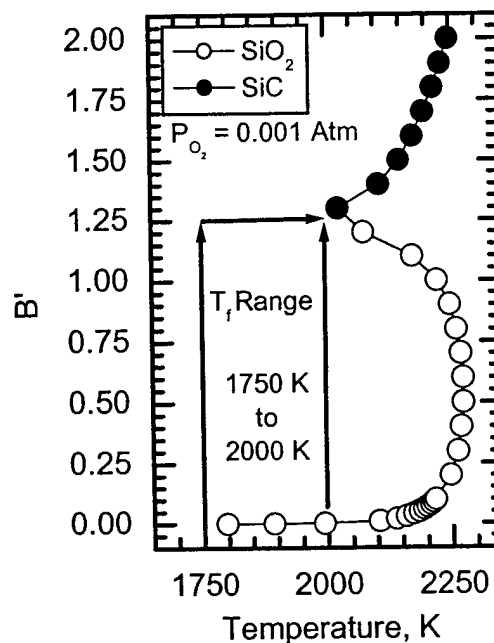

Figure 11. B' curve the O_2/SiC system at an oxygen pressure of 101 Pa.

Attempts have been made to extend the ACE methodology to include multiple surface constituents, in the MAT code. [31, 32] However, this requires additional assumptions to close the equation set, and efforts to match active-passive SiC oxidation data using the MAT code still rely on invoking a silica fail temperature. [31]

Working with an equilibrium surface chemistry model also presents other disadvantages. In particular, incorporating the effects of atomic oxygen on the oxidation process or on surface heating (through heterogeneous recombination) is not straightforward. At the moderate surface temperatures considered, equilibrium chemistry predicts very little atomic oxygen. Yet in flight, a large fraction of the oxygen traversing the boundary layer may be dissociated, and during arc-jet tests, as conducted in large facilities like the NASA Ames arc-jet complex, models are routinely subjected to air plasma streams in which the oxygen is completely dissociated. When O-atoms strike the surface, some will recombine to O_2 while others may oxidize the surface directly. The competition between these different surface processes is best described using rate equations.

For all of the reasons above, it seems advisable to replace the equilibrium thermochemistry model embodied by ACE with a finite rate chemistry formulation, such as presented by Zhluktov and Abe[33] for a carbon surface.

Summary

A computational model for simulating oxidation during transient aerothermal heating has been presented. The methodology and approach are discussed, and computational examples given for SiC oxidation. The computational examples demonstrate that the modified version of FIAT can simulate oxide growth and substrate recession during transient heating and pressure profiles, and can incorporate oxide dependent optical and thermal properties into the thermal response analysis.

Further model development is planned, including expansion of the oxidation model to include multi-component, multi-layer oxides, and the replacement of the equilibrium chemistry computations with a finite-rate chemistry formulation.

Acknowledgments

Appendix 1

The expressions given by Abelès's[23] contain several typographical errors and omissions; the corrected expressions are summarized below.
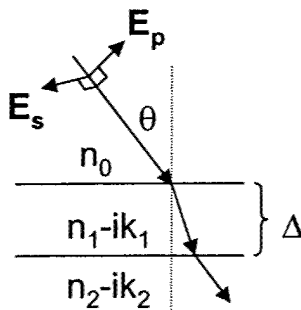

Figure A1. Model of three-layer thin film system

Figure A1 illustrates the thin film system considered. An s- or p-polarized light ray is incident at angle θ from a transparent medium into a thin absorbing layer of thickness Δ on an absorbing substrate. The refractive index of the transparent medium is n_0, the complex refractive index of the thin layer is $m_1 = n_1 - ik_1$ and the complex refractive index of the substrate is $m_2 = n_2 - ik_2$.

The reflectance is given by

$$R = \frac{ab\,e^{\kappa} + cd\,e^{-\kappa} + 2r\cos\eta + 2s\sin\eta}{bd\,e^{\kappa} + ac\,e^{-\kappa} + 2t\cos\eta + 2u\sin\eta} \quad (A1)$$

where:

$$\eta = \frac{4\pi n_1 \Delta}{\lambda}, \quad (A2)$$

$$\kappa = \frac{4\pi k_1 \Delta}{\lambda}, \quad (A3)$$

$$\begin{matrix} a \\ d \end{matrix} = [n_1 \mp n_0]^2 + k_1^2, \quad (A4)$$

$$\begin{matrix} b \\ c \end{matrix} = [n_1 \pm n_2]^2 + [k_1 \pm k_2]^2, \quad (A5)$$

$$\begin{matrix} r \\ t \end{matrix} = \left[n_0^2 - n_1^2 - k_1^2 + n_2^2 + k_2^2\right]\left[n_1^2 + k_1^2\right] \\ - n_0^2\left[n_2^2 + k_2^2\right] \mp 4n_0 k_1\left[k_1 n_2 - n_1 k_2\right], \quad (A6)$$

and

$$\begin{matrix} s \\ u \end{matrix} = 2k_1\left[n_2 \mp n_0\right]\left[n_1^2 + k_1^2 \pm n_0 n_2\right] \\ \pm 2k_2\left[k_1 k_2 n_0 \pm n_1\left[n_0^2 - n_1^2 - k_1^2\right]\right]. \quad (A7)$$

For normal incidence these expressions are equivalent to those given by Heavens[22]. For an oblique angle of incidence, the refractive indices must be replaced by their "effective" values, where

$$\begin{aligned} Y_0 &= n_0\cos\theta \\ Y_1 &= p_1 - iq_1 \\ Y_2 &= p_2 - iq_2 \end{aligned} \quad (A8)$$

for s-polarization and

$$Z_0 = n_0/\cos\theta$$
$$Z_1 = A_1 - iB_1 \qquad\qquad (A9)$$
$$Z_2 = A_2 - iB_2$$

for p-polarization, except in equation (A2) and A3) where n_1 and k_1 are always replaced by p_1 and q_1.

The real and complex parts of the effective refractive indices (i = 1,2) for s-polarization are calculated from solutions to the equation set

$$p_i q_i = n_i k_i$$
$$p_i^2 - q_i^2 = n_i^2 - k_i^2 - n_0^2 \sin^2\theta \qquad (A10)$$

For p-polarization the following relations are used.

$$A_i = p_i \left[1 + \frac{n_0^2 \sin^2\theta}{p_i^2 + q_i^2} \right]$$
$$\qquad\qquad (A11)$$
$$B_i = q_i \left[1 - \frac{n_0^2 \sin^2\theta}{p_i^2 + q_i^2} \right]$$

References

[1]Upadhya, K., Yang, J.-M., and Hoffman, W.P., "Materials for Ultrahigh Temperature Structural Applications", *The American Ceramic Society Bulletin*, Vol. 76, No. 12, 1997, pp. 51-56.

[2]Kaufman, L., "Boride Composites - A New Generation of Nose Cap and Leading Edge Materials for Reusable Lifting Re-entry Systems", AIAA Paper 70-278, February 1970.

[3]Clougherty, E.V., Pober, R.L., and Kaufman, L., "Synthesis of Oxidation Resistant Metal Diboride Composites", *Transactions of the Metallurgical Society of AIME*, Vol. 242, 1968, pp. 1077-1082.

[4]Tripp, W.C., Davis, H.H., and Graham, H.C., "Effect of an SiC Addition on the Oxidation of ZrB$_2$", *Ceramic Bulletin*, Vol. 52, No. 8, 1973, pp. 612-616.

[5]Talmy, I.G., Zaykoski, J.A., and Opeka, M.A., "Properties of Ceramics in the ZrB$_2$/ZrC/SiC System Prepared by Reactive Processing", *Ceramic Engineering and Science Proceedings*, Vol. 19, No. 3, 1998, pp. 104-112.

[6]Metcalfe, A.G., Elsner, N.B., Allen, D.T., Wuchina, E., Opeka, M., and Opila, E., "Oxidation of Hafnium Diboride", *Electrochemical Society Proceedings*, Vol. 99-38, 1999, pp. 489-501.

[7]Marschall, J., Chamberlain, A., Crunkleton, D., and Rogers, B., "Catalytic Atom Recombination on ZrB$_2$/SiC and HfB$_2$/SiC Ultrahigh Temperature Ceramic Composites", *Journal of Spacecraft and Rockets*, 2003, pp. In Press.

[8]Incropera, F.P., and DeWitt, D.P., *Fundamentals of Heat Transfer*, John Wiley & Sons, New York, 1981.

[9]Chen, Y.-K., and Milos, F.S., "Ablation and Thermal Response Program for Spacecraft Heatshield Analysis", *Journal of Spacecraft and Rockets*, Vol. 36, No. 3, 1999, pp. 475-483.

[10]Moyer, C.B., and Rindal, R.A., "An Analysis of the Coupled Chemically Reacting Boundary Layer and Charring Ablator, Part III. Finite Difference Solution for the In-Depth Response of Charring Materials Considering Surface Chemical and Energy Balances", NASA CR-1061, June 1968.

[11]Balat, M., Flamant, G., Male, G., and Pichelin, G., "Active to Passive Transition in the Oxidation of Silicon Carbide at High Temperature and Low Pressure in Molecular and Atomic Oxygen", *Journal of Materials Science*, Vol. 27, 1992, pp. 697-703.

[12]Hinze, J.W., and Graham, H.C., "The Active Oxidation of Si and SiC in the Viscous Gas-Flow Regime", *Journal of the Electrochemical Society*, Vol. 123, 1976, pp. 1066-1073.

[13]Gulbranson, E.A., Andrew, K.F., and Brassart, F.A., "The Oxidation of Silicon Carbide at 1150 to 1400 C and at 9x10^{-3} to 5x10^{-1} Torr Oxygen Pressure", *Journal of the Electrochemical Society*, Vol. 113, 1966, pp. 1311-1314.

[14]Rosner, D.E., and Allendorf, H.D., "High Temperature Kinetics of the Oxidation and Nitridation of Pyrolytic Silicon Carbide in Dissociated Gases", *Journal of Physical Chemistry*, Vol. 74, 1970, pp. 1829-1839.

[15]Narushima, T., Goto, T., Iguchi, Y., and Hirai, T., "High-Temperature Active Oxidation of Chemically Vapor-Deposited Silicon Carbide in an Ar-O$_2$ Atmosphere", *Journal of the American Ceramic Society*, Vol. 74, 1991, pp. 2583-2586.

[16]Vaughn, W.L., and Maahs, H.G., "Active-to-Passive Transition in the Oxidation of Silicon Carbide and Silicon Nitride in Air", *Journal of the American Ceramic Society*, Vol. 73, No. 6, 1990, pp. 1540-1543.

[17]Kendall, R.M., "An Analysis of the Coupled Chemically Reacting Boundary Layer and Charring Ablator, Part V. A General Approach to

the Thermochemical Solution of Mixed Equilibrium-Nonequilibrium Homogeneous or Heterogeneous Systems", NASA CR-1064, June 1968.

[18]Deal, B.E., and Grove, A.S., "General Relationship for the Thermal Oxidation of Silicon", *Journal of Applied Physics*, Vol. 36, 1965, pp. 3770-3778.

[19]Jacobson, N.S., "Corrosion of Silicon-Based Ceramics in Combustion Environments", *Journal of the American Ceramic Society*, Vol. 76, 1993, pp. 3-28.

[20]Norton, F.J., "Permeation of Gaseous Oxygen through Vitreous Silica", *Nature*, Vol. 191, 1961, pp. 701.

[21]Costello, J.A., and Tressler, R.E., "Oxidation Kinetics of Silicon Carbide Crystals and Ceramics: I, In Dry Oxygen", *Journal of the American Ceramic Society*, Vol. 69, No. 9, 1986, pp. 674-6781.

[22]Heavens, O.S., *Optical Properties of Thin Solid Films*, Dover Publications, Inc., New York, 1965.

[23]Abelès, F., "Optical Properties of Metallic Films", in *Physics of Thin Films*, M.H. Francombe and R.W. Hoffman, Editors, Academic Press, New York, 1971, pp. 151-204.

[24]Palik, E.D., ed. *Handbook of Optical Constants of Solids*, Academic Press, New York, 1985.

[25]Tropf, W.J., and Thomas, M.E., "Measurement and Estimation Techniques for High-Temperature Radiative Properties of Solids", in *American Society of Mechanical Engineers, Technical Publishing Pamphet Paper, 95-WA/JHT-31*, ASME Technical Publishing, New York, 1995, pp. 1-10.

[26]Saunders, D., Allen, G., Gage, P., and Reuther, J., "Crew Transfer Vehicle Trajectory Optimization", AIAA Paper 2001-2885, June 2001.

[27]Bargeron, C.B., Benson, R.C., Jette, A.N., and Phillips, T.E., "Oxidation of Hafnium Carbide in the Temperature Range 1400 to 2060 C", *Journal of the American Ceramic Society*, Vol. 76, 1993, pp. 1040-1046.

[28]Bargeron, C.B., Benson, R.C., Newman, R.W., Jette, A.N., and Phillips, T.E., "Oxidation Mechanisms of Hafnium Carbide and Hafnium Diboride in the Temperature Range 1400 to 2100 C", *Johns Hopkins APL Technical Digest*, Vol. 14, 1993, pp. 29-35.

[29]Holcomb, G.R., and St. Pierre, G.R., "Application of a Counter-Current Gaseous Diffusion Model to the Oxidation of Hafnium Carbide at 1200 to 1530 C", *Oxidation of Metals*, Vol. 40, No. 1/2, 1993, pp. 109-118.

[30]Galanov, B.A., Ivanov, S.M., Kartuzov, E.V., Kartuzov, V.V., Nickel, K.G., and Gogotsi, Y.G., "Model of Oxide Scale Growth on Si_3N_4 Ceramics: Nitrogen Diffusion through Oxide Scale and Pore Formation", *Computational Materials Science*, Vol. 21, 2001, pp. 79-85.

[31]Milos, F.S., and Chen, Y.-K., "Comprehensive Model for Multicomponent Ablation Thermochemistry", AIAA Paper 97-0141, January, 1997.

[32]Milos, F.S., and Marschall, J., "Thermochemical Ablation Model for TPS Materials with Multiple Surface Constituents", AIAA Paper 94-2042, June 1994.

[33]Zhluktov, S.V., and Abe, T., "Viscous Shock-Layer Simulation of Airflow past Ablating Blunt Body with Carbon Surface", *Journal of Thermophysics and Heat Transfer*, Vol. 13, No. 1, 1999, pp. 50-59.

Microhardness and high-velocity impact resistance of HfB$_2$/SiC and ZrB$_2$/SiC composites

J. MARSCHALL
Molecular Physics Laboratory, SRI International, Menlo Park, CA 94025, USA

D. C. ERLICH
Materials Research Laboratory, SRI International, Menlo Park, CA 94025, USA

H. MANNING, W. DUPPLER
Physics Department, Concordia College, Moorhead, MN 56562, USA

D. ELLERBY
Thermal Protection Materials and Systems Branch, NASA Ames Research Center, Moffett Field, CA 94035, USA

M. GASCH
ELORET Corp. at NASA Ames Research Center, Moffett Field, CA 94035 USA

Abstract

The results of Vickers microhardness and high-velocity impact tests on monolithic ZrB$_2$/SiC and HfB$_2$/SiC ultra-high temperature ceramic (UHTC) composites are presented. The UHTC materials exhibit fracture behavior typical of ceramics under indentation and impact loading. The materials are relatively hard with microhardness values of about 15 to 20 GPa. Cracks were observed to extend from the corners of indentations. Impacts of stainless steel and tungsten carbide spheres, with diameters in the 500 to 800 micron range and velocities of 200 to 300 m/s, produced minimal plastic deformation but significant radial and ring cracking at the impact sites. Impacts of micron-scale iron particles traveling at 1 to 3 km/s produced essentially no surface damage.

1

1. Introduction

Hypersonic flight vehicle designs incorporating sharp leading edges have many potential advantages over traditional blunt-body designs. These advantages derive primarily from higher lift to drag ratios that translate into increased cross-range capability, improved high-speed maneuverability, better landing characteristics, and a greater ability to fly abort or emergency trajectories. As one example, recent modeling studies comparing the performance of blunt-body and sharp-body designs for a crew transfer vehicle to ferry astronauts between the Earth and the International Space Station found dramatic performance benefits for the sharp-body design [1,2].

Sharp leading edges experience intense aerothermal heating that few materials can survive. Monolithic ultra-high temperature ceramic (UHTC) composites based on ZrB_2 and HfB_2 offer a potential solution. Both the diborides and their primary metal oxides have extremely high melting points [3]. UHTC composites have shown good dimensional stability in low-pressure supersonic aerothermal heating environments, where other refractory materials rapidly fail by melting, spalling, pyrolyzing or ablating [4]. Several studies have demonstrated that the high-temperature oxidation/ablation resistance of diboride-based UHTC materials is enhanced by the addition of SiC [5-9], with optimum performance achieved around 20 volume percent SiC. UHTC leading edge components were flown by NASA in two separate hypersonic flight tests, SHARP-B1 (1997; UHTC nose tip)[10,11] and SHARP-B2 (2000; UHTC strakes).

In this paper, we present the results some preliminary experiments exploring the hardness and impact resistance of UHTC materials. Impact damage is a major concern for any leading edge component, since leading edges are exposed to the most severe aerothermal environments and directly influence vehicle flight characteristics. A very large spectrum of possible impacts exists, ranging from tool drops, to collisions with high velocity debris during take-off and landing, to hypervelocity impacts with micrometeorites and "space junk" while in-orbit. We sample some of these impact conditions, using a compressed gas gun to fire steel and tungsten carbide balls with diameters of ~0.5 mm at velocities in the 100 – 300 m/s range, and a 2 MV Van de Graaff particle accelerator to fire micron-scale iron particles in the 1-3 km/s range. We document the results using optical and scanning electron microscopy.

2. Experimental Procedure

2.1. UHTC Materials

Experiments were conducted on two UHTC compositions: ZrB_2 with 20 volume percent SiC and HfB_2 with 20 volume percent SiC. The former composition has a density of ~ 5.5 g/cm^3 and latter of ~9.5 g/cm^3. For brevity, these two compositions are referred to as ZrB_2/SiC and HfB_2/SiC throughout the text. UHTC materials are manufactured from diboride and silicon carbide powders, by hot pressing. All materials were supplied by NASA Ames Research Center, either from remaining stock manufactured during the SHARP-B1 and SHARP-B2 programs by commercial vendors, or from newer material manufactured in-house at NASA Ames. The former materials are referred to as "heritage" materials and the later as "current" materials in the text. Test samples were machined from the billets using diamond cutting and grinding operations, and polished using diamond powder.

2

2.2. Microhardness Measurements

The Vickers microhardness of UHTC samples was measured at SRI using a Leitz Durimet Small-Hardness tester and at NASA Ames using a Shimadzu HSV-30 hardness tester. Measurement consistency between the two hardness testers was verified experimentally. Measurements at SRI were made with a constant load of 19.6 N (2kg mass), while data at NASA Ames was gathered under a variety of loads ranging from 1.96 N to 294 N (0.2 kg – 30 kg mass). Indentations were examined using optical and scanning electron microscopy.

2.3. Gas Gun Impact Experiments

UHTC samples were impacted with tungsten carbide or stainless steel balls using a compressed gas gun. Type 44A tungsten carbide (WC) balls with diameters of 794 μm (1/32 inch) and 508 μm (0.020 inch), and type 440-C stainless steel (SS) balls with diameters of 508 μm (0.020 inch) and 762 mm (0.030 inch), were used. The tolerances on ball diameters are ±5 μm. Type 44A WC contains 6 % cobalt by weight. Both materials are magnetic. The pertinent physical properties of these balls are given in Table I.

Figure 1 shows the essential components of the gas gun apparatus. A single ball is placed into the gun barrel and held in place by a magnet. The ball is accelerated down the barrel by the sudden release of a compressed gas (nitrogen). The gas is released either by opening a valve or by rupturing a thin diaphragm separating the barrel from a compressed gas reservoir. The accelerated ball is sequentially detected by three photodiodes as it travels down the gun barrel, and its velocity is calculated from the measured time intervals and the known photodiode spacing. Velocities are varied by changing the type and thickness of the diaphragm or by adjusting the pressure in the gas reservoir.

2.4. Particle Accelerator Impact Experiments

The resistance of UHTC samples to hypervelocity impact by micron-sized iron particles was explored using a 2 MV Van de Graaff particle accelerator located at Concordia College, in Moorhead, Minnesota. Figure 2 shows a schematic diagram of the particle accelerator. Particles are loaded into an injector inside the Van de Graaff ball. The injector agitates the dust, generating a dust cloud. Some particles contact a sharp needle maintained at high voltage and acquire a large positive charge. These particles are then focused, injected into the electric field of the Van de Graaff, and accelerated downstream. After leaving the Van de Graaff ball, the particles travel through a field-free drift tube, where sensors measure the velocity and charge of individual particles. Knowledge of these quantities together with the accelerator voltage allow calculation of the particle mass, and for spherical particles with a known density, the particle diameter. A test chamber is positioned at the end of the flight tube, where particles are directed at a target for impact testing. Particles not meeting user-chosen specifications of charge and velocity can be deflected before entering the test chamber.

Efficient particle charging and acceleration requires conductive particles. Past experience has shown that micron-sized iron particles, manufactured from iron carbonyl by a reduction process, work well in the accelerator. Such particles were also used in the present tests. Unfortunately, the carbonyl reduction process results in substantial particle porosity and

3

somewhat uncertain particle density in the 4 to 6 g/cm^3 range. The hardness of these particles is also uncertain.

3. Results

3.1. Microhardness Measurements

Vickers microhardness measurements were made at SRI on heritage HfB$_2$/SiC and ZrB$_2$/SiC specimens. Fifteen individual measurements were made at a load of 19.6 N on each specimen and examined optically. Average microhardness values were 20.5 ± 1.6 GPa for the HfB$_2$/SiC sample and 18.1 ± 1.0 GPa for the ZrB$_2$/SiC sample. A typical impression on ZrB$_2$/SiC is shown in the SEM image of Fig. 3. Cracks are observed to extend from the indentation corners and some chipping is seen along indentation edges. The extent of cracking was generally less, and the extent of chipping more, in the HfB$_2$/SiC specimens. Cracks propagate both around and through individual grains, while chipping appears to be associated mainly with failure along grain boundaries.

A series of Vickers microhardness indentations were made as a function of load at NASA Ames Research Center on two samples of current HfB$_2$/SiC material. Impressions produced under a 9.81 N load have indentation diagonals on the order of 30 μm. At lower loads, impression dimensions begin to approach the scale of the microstructure and are highly distorted by cracking or chipping of individual grains. Hardness values did not vary significantly or systematically with increasing loads above 9.81 N. Averaging the measurements obtained at 9.81 N, 29.4 N, 49 N, 98.1 N, and 294 N, gives 16.3 ± 0.4 GPa and 15.4 ± 0.3 GPa for the two HfB$_2$/SiC specimens. The current HfB$_2$/SiC material appears to be somewhat softer than the heritage material, though still quite hard by comparison to most other materials.

Our microhardness values can be compared with various data reported in the literature for ZrB$_2$, HfB$_2$ and SiC, and summarized in Table II. Our measured microhardness values for the ZrB$_2$/SiC and HfB$_2$/SiC composites are generally lower than literature values for the individual constituents.

3.2. Gas Gun Impact Results

Fifty-five separate shots were fired at normal incidence at 14 different UHTC samples. Not all of the shots could be correlated to damage on the surface. Generally, impact velocities of ~ 200 m/s on ZrB$_2$/SiC and ~250 m/s on HfB$_2$/SiC were required before impact sites could be positively identified on polished specimens using optical microscopy or SEM imaging. Only one of the nine impacts below these velocity thresholds was identified, a 94 m/s, 794 μm WC sphere impact on ZrB$_2$/SiC. While impact damage below these velocity thresholds is likely, the difficulty in locating and identifying such impact site also reflects the limited surface damage done to these materials at the lower impact velocities.

Figure 4 shows an impact site produced by a 794 μm WC ball striking a heritage ZrB$_2$/SiC specimen at 308 m/s. A concentric ring crack pattern is formed and radial cracks extend outward. These types of cracking patterns are the major visual indicators of impact damage. No evidence of UHTC material removal by fragmentation was found. The dark objects surrounding the impact site were confirmed by EDX analysis to be fragments from the impacting WC ball.

4

The largest ring crack diameter in Fig. 4 is about 500 μm. Myriad concentric ring cracks lie within this bounding diameter. SEM images of this area show tightly spaced ring cracks that appear as thin, white traces with no visible separation between adjacent surfaces; see Fig. 5. The concentric ring pattern suggests displacements into the surface to accommodate the spherical particle impact. The lack of separation between adjacent crack surfaces suggests a locally compressive stress field normal to the surface traces.

In contrast, radial cracks generally appear more open, with mating surfaces visibly separated, suggesting a local tensile stress. Figure 6 shows an SEM image of a radial crack extending from the outer ring crack pattern. Though difficult to trace to their terminus, many radial cracks were observed to extend at least 2 to 5 times the outer ring crack diameter.

The nature and extent of the crack patterns generated around impact sites varies. Figure 7 summarizes the diameters of the outer most ring crack observed on ZrB_2/SiC and HfB_2/SiC surfaces as a function of velocity for impacting spheres with different sizes and compositions. Similar plots can be made as a function of impact momentum and kinetic energy. Measurements of crack dimensions are somewhat subjective, but some general observations can be made.

Impacts by balls of comparable size, composition and velocity produced more extensive damage to ZrB_2/SiC than to HfB_2/SiC, as reflected by the quantity and extent of the observed surface cracks.

Impacts with stainless steel spheres left fundamentally different surface patterns than tungsten carbide spheres. Instead of numerous concentric ring cracks, as seen in Fig. 4, stainless steel impacts typically produced a single prominent ring crack, as shown in Fig. 8. The ring crack in Fig. 8 is a perfect 595 μm diameter circle. Only for the highest velocity impacts, on ZrB_2/SiC, was there any evidence of multiple ring cracks produced by stainless steel impacts, and the additional cracks were still bounded by a prominent outer ring crack.

None of the stainless steel impacts produced observable radial cracks on either ZrB_2/SiC or HfB_2/SiC surfaces. Neither did impacts of 508 μm WC spheres on ZrB_2/SiC. The formation of radial cracks evidently requires more energetic impacts than the formation of ring cracks. In our experiments only the highest speed impacts (over ~ 250 m/s) with the large WC balls produced radial cracks that extend away from the concentric ring crack pattern.

A computer-controlled scanning laser confocal microscope [12] was used to obtain orthogonal surface profiles of impressions made by 310 m/s impacts of 794 μm diameter WC spheres on ZrB_2/SiC and HfB_2/SiC; see Fig. 9. These profiles reveal greater residual deformation in the ZrB_2/SiC specimen. The profiles show more extrusion of material around the impact on the ZrB_2/SiC surface, and the impression depth in the ZrB_2/SiC is 30% to 40% greater than in the HfB_2/SiC. These findings are in line with the qualitative observation that impressions made by comparable impacts were easier to detect visually using oblique illumination on the ZrB_2/SiC specimens.

The effect of impact damage on biaxial flexural strength was examined by testing three impacted disks of current HfB_2/SiC material using a standard concentric ring flexural test as described in ASTM standard C 1499-03 [13]. Each disk was impacted with a single 794 mm diameter WC ball, the first at 312 m/s, the second at 206 m/s and the third at an unknown velocity below 100 m/s. The first two disks had an as-ground surface finish, while the latter was polished.

The first and second impacted specimens exhibited fracture strengths of 195 MPa and 226 MPa, respectively. These two values are well below 426 ± 48 MPa, the average fracture strength and standard deviation determined for five un-impacted as-ground test samples. Both the first and second specimen failed in the region of the impact. The third impacted specimen failed in a normal manner directly under the compression ring center, with measured fracture strength of 458 MPa. This value is comparable to 487 ± 35 MPa, the average fracture strength and standard deviation measured for five un-impacted polished test samples.

All fractures were clean from processing defects, agglomerates, and inclusions. The test results suggest that microcrack formation, induced by particle impact, weakened the first and second specimens noticeably, while the impact velocity was too low to cause significant damage to the third specimen.

3.3. Particle Accelerator Impact Results

Several HfB_2/SiC and ZrB_2/SiC specimens were impacted at normal and oblique incidence by carbonyl iron particles with diameters around 1 micron traveling at speeds around 1.8 km/s. Table III summarizes the pertinent experimental parameters for these tests.

At normal incidence, particle impacts, detected by SEM in the form of surface abnormalities, were found on both the ZrB_2/SiC and the HfB_2/SiC specimens. Many more residual iron particles were found on ZrB_2/SiC than HfB_2/SiC, though this discrepancy may partially reflect the greater number of particles fired at the former specimen. Figure 10 shows an example of two such impact sites on ZrB_2/SiC. Visually, these sites appear to show deformed iron particles that have adhered to the specimen surface. Stereo images of various impact sites, produced from SEM micrographs obtained at different specimen tilt angles, indicate that the impact features extend above the sample surface.

Figure 10 also shows local EDX spectra taken at the four different locations on the impact sites as indicated in the SEM micrograph. The prominent iron peaks at sites 1, 2, and 3 confirm that the impact features are indeed residual iron particles. The EDX technique probes a surface depth on the order of a micron. Si and Zr peaks associated with the surface material beneath the residual iron are also present, suggesting that residual iron layer is considerably thinner than a micron.

Unambiguous detection of impact damage to UHTC specimens was difficult. No extended damage, such as surface cracks emanating from impact sites, was ever observed. At most sites the UHTC materials seem completely unaffected by the impact. In some cases, like location 3 in Fig. 10, the central region of an impact site exhibits a "fragmentary" pattern that suggests impact damage to the UHTC. However, EDX spectra of these regions show strong iron signals, so it seems more likely the patterns reflect the deformation of impacting iron particles rather than damage to the UHTC below. Nevertheless, some damage to UHTC material was occasionally found. For, example, the EDX spectrum taken at location 4 shows no iron peaks and strong Zr and B peaks, suggesting a ZrB_2 fragment was created during the impact.

At oblique incidence, no particle impacts could be detected. The location of oblique impact sites by SEM is expected to be more difficult, since the impacts are spread out over a larger target area (~ 3 times larger for an incident angle of 70°.) However, for the ZrB_2/SiC experiments, the diluting effect of the increased target area was largely offset by doubling the

6

number of impacting particles. Therefore, it seems more likely that particles are deflected by their oblique collisions with the surface.

In a further experiment, a ZrB_2/SiC specimen was impacted at normal incidence in two separate locations by approximately 100 particles traveling either 1.0 to 1.3 km/s or greater than 2 km/s. Some impact sites, such as the left impact in Fig. 10, show droplet features that hint at melting. A simple analysis indicates that about 1.25 MJ/kg of thermal energy will completely melt an iron particle initially at room temperature. Iron particles traveling faster than ~1.6 km/s generally posses kinetic energies per mass in excess of this value. For the slow particle group, the specific kinetic energy ranged from 0.43 to 0.89 MJ/kg and for the fast group 1.9 to 5.0 MJ/kg. SEM and EDX observations revealed numerous impact sites with adhering iron material for the slower particles, but none for the faster particles. Thus complete particle melting is not required for surface adhesion and higher impact velocities seem to prevent iron remnants from adhering to the surface.

4. Discussion

The response of ZrB_2/SiC and HfB_2/SiC samples to indentation and particle impact is typical of that observed for ceramics and glasses [14-16]. For point contact on brittle solids, the loading phase typically leads to the formation and growth of a small, highly deformed plastic zone from which median vent cracks are nucleated and extended. The unloading phase results in the additional formation and extension of lateral vent cracks, and closing of the median cracks [14,17,18]. The intersection of the median vent cracks with the surface produces radial cracking patterns. The extension and breakout to the surface of lateral vent cracks can lead to significant fragmentation and chipping. For indentation with a Vickers indenter on isotropic solids, the sharp edges of the pyramidal indenter tend to align median vent cracks with the indentation diagonals and tend to promote more extensive radial cracking [15]. The unloading of a pyramidal indenter also leads to closure of median cracks beneath the indentation, however the near surface region generally experiences tensile stresses that tend to open up and extend radial cracks [15,19].

Although we do not observe median vent crack formation directly, radial cracks emerging from impression corners are a ubiquitous feature of Vickers indentations on ZrB_2/SiC and HfB_2/SiC samples. No evidence of lateral vent cracks intersecting the surface was found. When chipping was observed, it was in the immediate indentation area and could be associated with the pop-out of individual grains or local fracture around several grains. The emergence of lateral cracks to the surface would be expected at larger distances from the impression and would result in larger fragments than observed.

Contact between a hard blunt indenter and a flat isotropic brittle material can result in loading conditions that are essentially elastic. Under such conditions, Hertzian cone cracks can form, initiating at the surface as ring fractures and then propagating into the material along conical trajectories [20,21]. Under large concentrated contact pressures, such as for small spherical indenters, plastic deformation may also occur, inhibiting cone cracking and generating the crack types usually associated with sharp indenters [15,22]. The cracking patterns generated by high-speed impact of spherical particles in the 100's of m/s range are very similar to those found under blunt indenters [15,20,22,23].

The damage observed on ZrB_2/SiC and HfB_2/SiC surfaces for tungsten carbide and stainless steel sphere impacts clearly indicates that loading stresses on the target were predominately

7

elastic. Cone cracking, as evidenced by surface ring crack patterns, is the major fracture mode and is certainly not inhibited by the formation of a plastic zone. The impressions left by impacts are extremely shallow when compared to the size of the impacting spheres. The ratio of impression depth to impacting sphere radius is on the order of 1 to 400 for the profiles shown in Fig. 9, indicating little permanent deformation in the UHTC samples to accommodate the impact stresses. The minimal permanent deformation that is seen is plausibly explained as displacement of material into the surface along cone crack trajectories. The appearance of radial cracks at higher velocities is likely associated with tensile surface hoop stresses formed during unloading.

Formulae based on Hertzian elastic contact theory can be used to estimate the contact radius at maximum load between an impacting sphere and a flat specimen [22]:

$$a = \left(\frac{4}{3}kF_{max}R\right)^{1/3} \tag{1}$$

where

$$F_{max} = \left(\frac{5}{3}\pi\rho\right)^{3/5}\left(\frac{3}{4}k\right)^{-2/5}V^{6/5}R^2 \tag{2}$$

and

$$k = \left(\frac{1-v^2}{E} + \frac{1-v_{UHTC}^2}{E_{UHTC}}\right) \quad . \tag{3}$$

In these expressions, a is the contact radius, F_{max} is the maximum load, R is the sphere diameter, ρ is the sphere density, V is the sphere velocity and k is a constant related to the Poisson's ratios v, v_{UHTC} and the Young's moduli E, E_{UHTC} of the sphere and the specimen, respectively.

The ZrB$_2$/SiC and HfB$_2$/SiC materials both have Poisson's ratios of about 0.15 and Young's moduli [24] of about 530 GPa. Therefore, the predicted contact radius and maximum load are the same on both UHTC compositions for comparable sphere impacts. A contact radius of approximately 18 μm is calculated for the 310 m/s WC impacts profiled in Fig. 9. This is an order of magnitude smaller than the radii of the outer ring cracks generated during the impacts.

Though the contact radius and maximum load are identical, impacts of tungsten carbide spheres generate more extensive ring cracks in ZrB$_2$/SiC than in HfB$_2$/SiC at a given velocity. The maximum radial tensile surface stress generated at a distance r from the impact site is given by [22]

$$\sigma_{r,max} = \frac{(1-2v_{UHTC})F_{max}}{2\pi r^2} \quad . \tag{4}$$

If the assumption is made that the outermost ring crack forms where the radial surface stress just exceeds a critical value characteristic of the material, the ratio of critical stresses for the two UHTC formulations can be estimated from

$$\frac{\sigma_{c,HfB_2/SiC}}{\sigma_{c,ZrB_2/SiC}} \cong \frac{\left(\dfrac{V^{6/5}R^2}{r_c^2}\right)_{ave,HfB_2/SiC}}{\left(\dfrac{V^{6/5}R^2}{r_c^2}\right)_{ave,ZrB_2/SiC}} \quad . \tag{5}$$

From the outer ring diameters plotted in Fig. 7 this ratio is about 1.6 ± 0.2.

8

These computations are only approximate, of course. Some of the available kinetic energy is dissipated in the deformation and fracture of the impacting sphere. Since the heritage HfB_2/SiC is about 1.7 times denser and slightly harder than the heritage ZrB_2/SiC material, it is likely that impacts on HfB_2/SiC result in more energy dissipation into the impacting sphere.

This is very apparent for the SS sphere impacts, which predominately generate a single large ring crack, as shown in Fig. 8. A Rockwell C hardness of 58 to 65 equates approximately to a Vickers hardness of 6.5 to 8 GPa [25], making the stainless steel balls significantly softer than both the heritage ZrB_2/SiC and HfB_2/SiC materials. This must lead to extensive deformation (flattening) of the sphere upon impact. The SS spheres are less dense than, and have the largest hardness discrepancy with the HfB_2/SiC material. For comparable SS impacts, the ring crack diameters are observed to be larger on the HfB_2/SiC material than the ZrB_2/SiC material. This suggests greater deformation of the SS sphere upon impact on the harder and denser material, resulting in a larger contact radius before critical radial surface stress for ring crack formation is exceeded.

A similar deformation mechanism can be invoked to explain the relative lack of surface damage from the micron-scale carbonyl iron particle impacts in the 1 to 3 km/s range. That is, the impact energy is largely dissipated in the deformation and melting of the iron particle, rather than into the UHTC. The density of these iron particles is even lower than that of the SS spheres, and while their hardness is not known exactly, they are likely softer than the UHTC materials.

5. Conclusions

The major findings of this study can be summarized as follows:

1. UHTC materials are relatively hard, with Vicker's hardness numbers in the 15-20 GPa range. Cracks are observed to emanate from indentation corners.

2. Impacts by 508 μm and 794 μm WC spheres traveling at several 100 m/s produce surface damage observable as patterns of ring and radial cracks. Similar impacts by SS spheres produced considerably less damage.

3. The observed formation of cracks during indentation and particle impact is consistent with damage modes documented for other ceramic materials under similar conditions.

4. Biaxial testing of impacted HfB_2/SiC specimens indicates that impact damage of this sort can cause large decreases in fracture strength.

5. Impacts of micron-sized iron particles traveling at 1 to 3 km/s were shown to cause insignificant damage to UHTC surfaces.

Finally, we note that the experiments presented here are of an exploratory nature. Compared to many other ceramics and glasses, very little is actually known about the impact damage and fracture resistance of ZrB_2/SiC and HfB_2/SiC materials. Further focused investigations should be made to systematically quantify the effect of contact and impact damage on the strength and reliability of UHTC components. The influence of temperature on impact damage should be investigated, since UHTC leading edges will cool well below room temperature on orbit and reach very high surface temperatures during hypersonic flight. Impact experiments with projectiles at orbital velocities ($\sim$ 8 km/s) and above are certainly required to properly assess the risks of imposed by micrometeorites and orbital debris to critical UHTC leading edge

9

components. Finally, the fracture strength degradation observed for the impacted HfB$_2$/SiC specimens argues strongly for a more extensive testing program to quantify impact induced strength degradation.

Acknowledgements

Tables

TABLE I Physical properties of tungsten carbide and stainless steel spheres.[a]

	WC 44A	SS 440-C
ρ (g/cm^3)	14.95	7.67
ν	0.26	0.29
E (Gpa)	690	200
H_R	C58-C65	A90.5-A91.5

[a] Manufacturer data; New England Miniature Ball Corporation (www.nemb.com)

TABLE II Published microhardness values for ZrB$_2$, HfB$_2$ and SiC.

Material	Microhardness (GPa)	Comments
ZrB$_2$	35.0 [a]	Vickers, polycrystal
	29.4 [b]	Vickers, 50 g load, single grains
	~25-30 [c]	Knoop, single crystal, anisotropic effects
	22.1 [d]	---------
HfB$_2$	31.4 [b]	Vickers, 50 g load, single grains
	~25-30 [c]	Knoop, single crystal
SiC	31.0 [a]	Vickers, single crystal
	27.0 [a]	Vickers, polycrystal
	28.2 [d]	Knoop, 25 g load
	27.2 [e]	Vickers, 500 g load, sintered α-SiC
	25 [f]	Knoop, load-independent, 6H-SiC film

[a] Milman et al. [26]; [b] Bsenko and Lundström [27]; [c] Nakano et al. [28]; [d] Glazov and Vigdorovich [29]; [e] Quinn et al. [30]; [f] Kakanakova-Georgieva et al. [31].

TABLE III Experimental parameters for UHTC impact tests using the Van de Graaff particle accelerator.

	Test 1	Test 2	Test 3	Test 4
Specimen	HfB_2/SiC	HfB_2/SiC	ZrB_2/SiC	ZrB_2/SiC
Incident Angle (deg)	0	70	0	70
Number of Shots	200	150	400	800
Velocity (km/s)				
Average	1.75 ± 0.46	1.87 ± 0.46	1.76 ± 0.72	1.82 ± 0.47
Median	1.66	1.82	1.66	1.74
Mass (pg)				
Average	44.4 ± 61.5	28.5 ±36.8	49.2 ± 66.04	38.8 ±53.2
Median	25.3	15.5	27.0	20.6
Kinetic Energy (nJ)				
Average	45 ± 38	35 ± 29	48 ± 40	42 ± 37
Median	37	28	36	32

Figure Captions

Figure 1 Gas gun impact apparatus.

Figure 2 Van de Graaff particle accelerator.

Figure 3 SEM image of a Vickers microhardness impression on heritage ZrB_2/SiC. Light grains are ZrB_2 and dark grains SiC.

Figure 4 Optical microscope image of surface damage produced on a heritage ZrB_2/SiC surface by the 308 m/s impact of a 794 μm diameter tungsten carbide ball.

Figure 5 SEM image of ring crack pattern on ZrB_2/SiC surface; same impact as Fig. 4..

Figure 6 SEM image of a radial crack at boundary of ring crack pattern on ZrB_2/SiC surface; same impact as Fig. 4.

Figure 7 Summary of outer ring crack diameters observed on ZrB_2/SiC and HfB_2/SiC surfaces as a function of size, composition, and velocity of the impacting ball.

Figure 8 Optical microscope image of the ring crack generated by the 316 m/s impact of a 762 μm diameter stainless steel ball on a HfB_2/SiC surface.

Figure 9 Orthogonal surface profiles through the centers of impressions produced by 310 m/s impacts of 794 μm diameter WC spheres on ZrB_2/SiC and HfB_2/SiC surfaces. Profiles are separated by arbitrary elevation offsets for clarity.

Figure 10 SEM micrograph showing two impact sites of micron-sized carbonyl iron particles on a ZrB_2/SiC surface, along with the EDX spectra obtained at the four locations indicated.
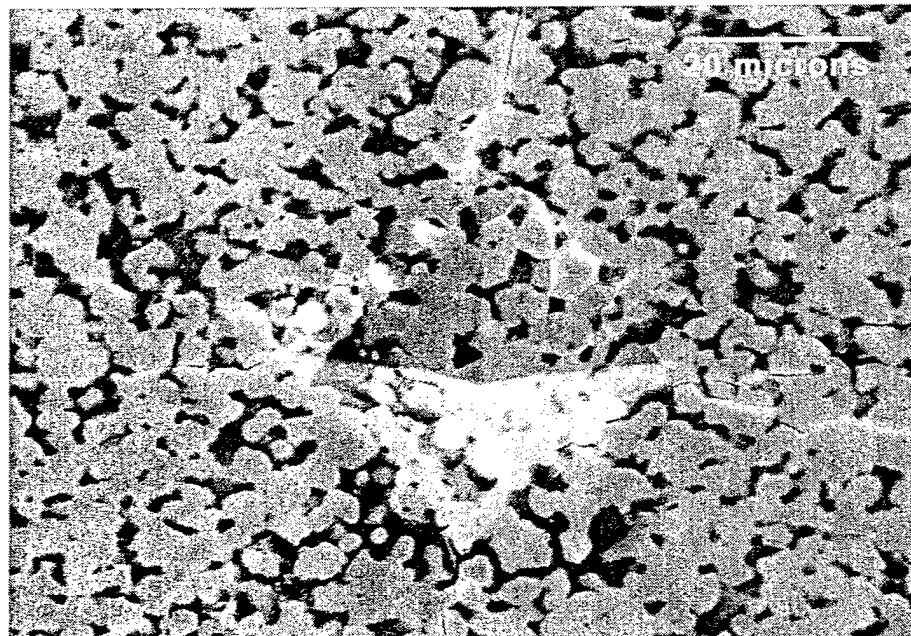
Figures

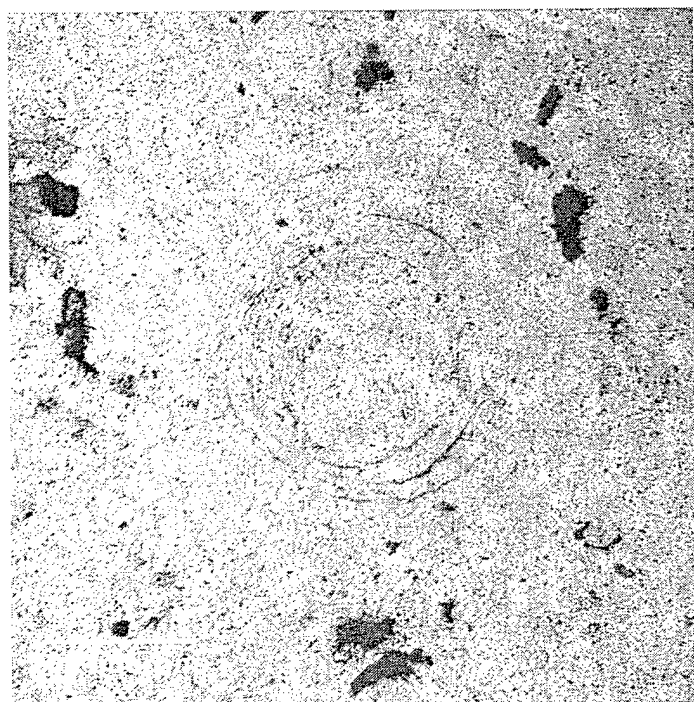Figure 1

VdG Ball

Dust Injector

Diffusion Pump

Alignment Grids

Particle Detectors

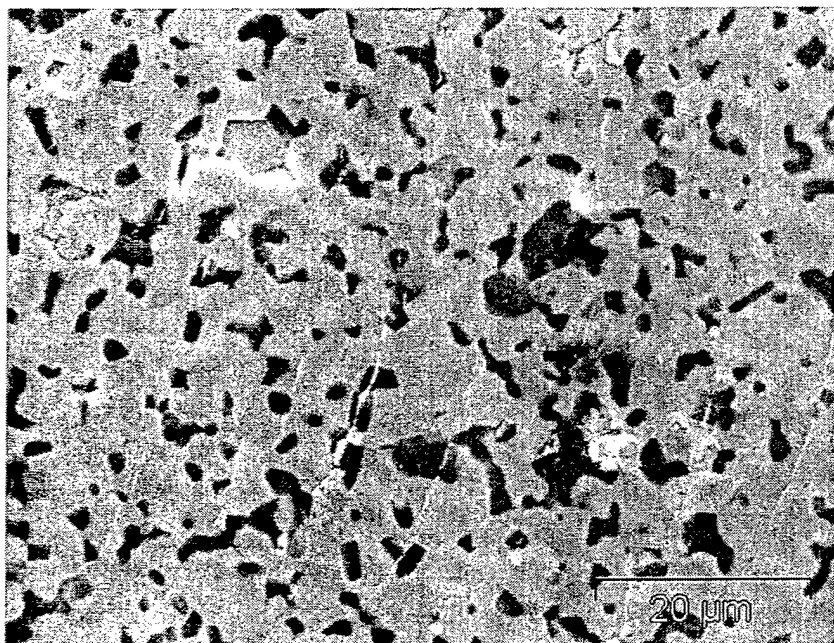Particle Deflection Electrodes
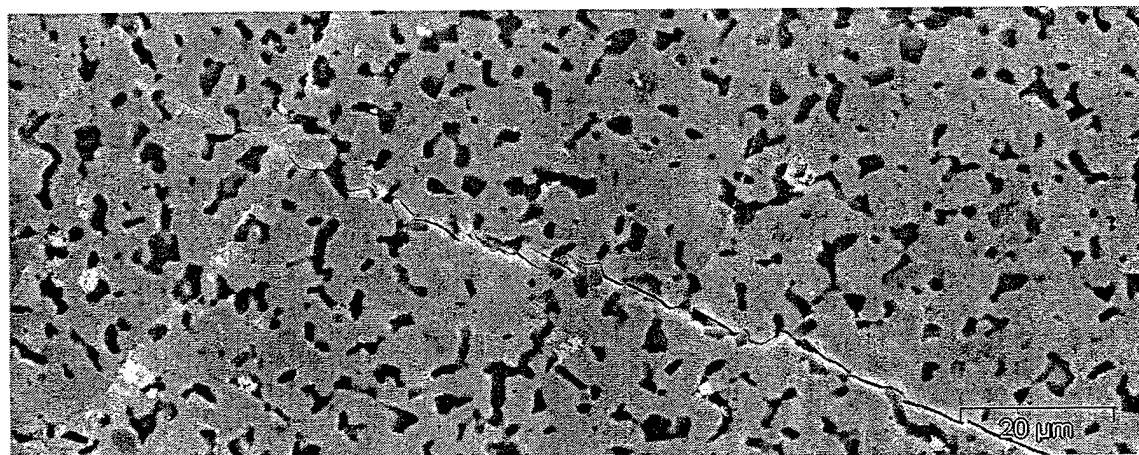
Experimental Chamber

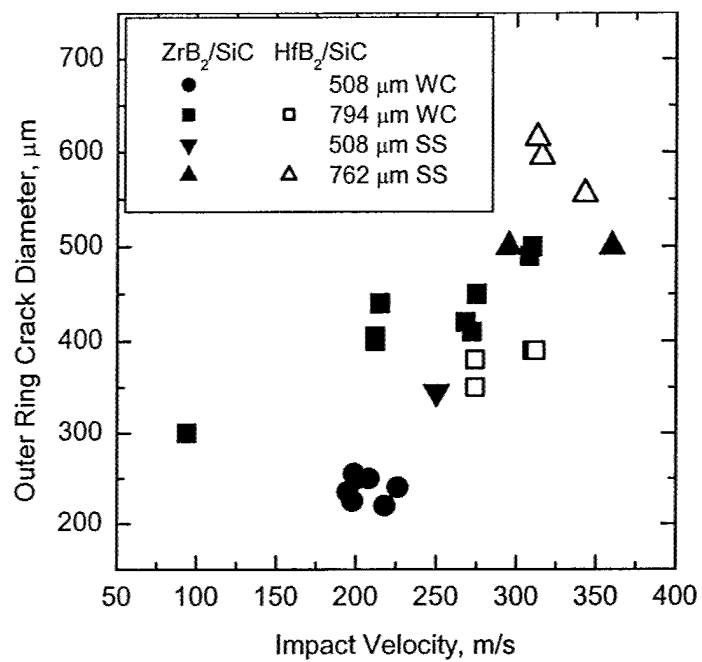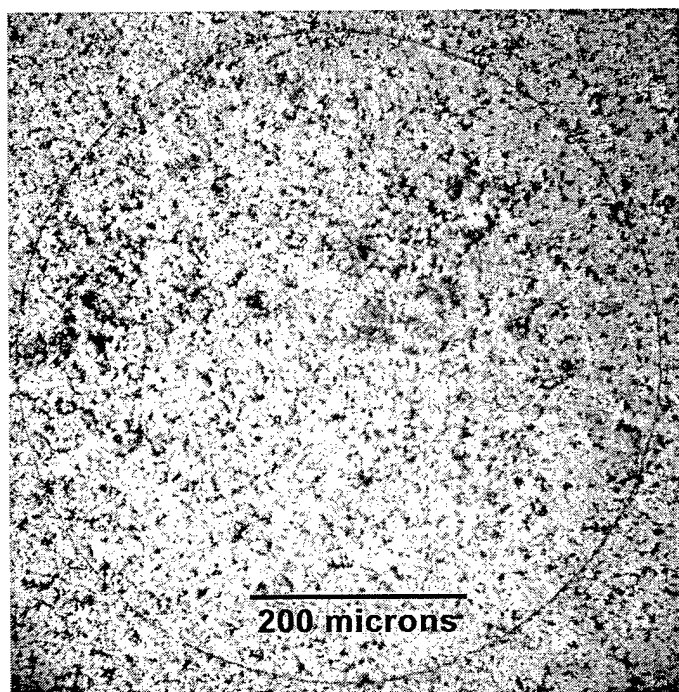Mechanical Vacuum Pump
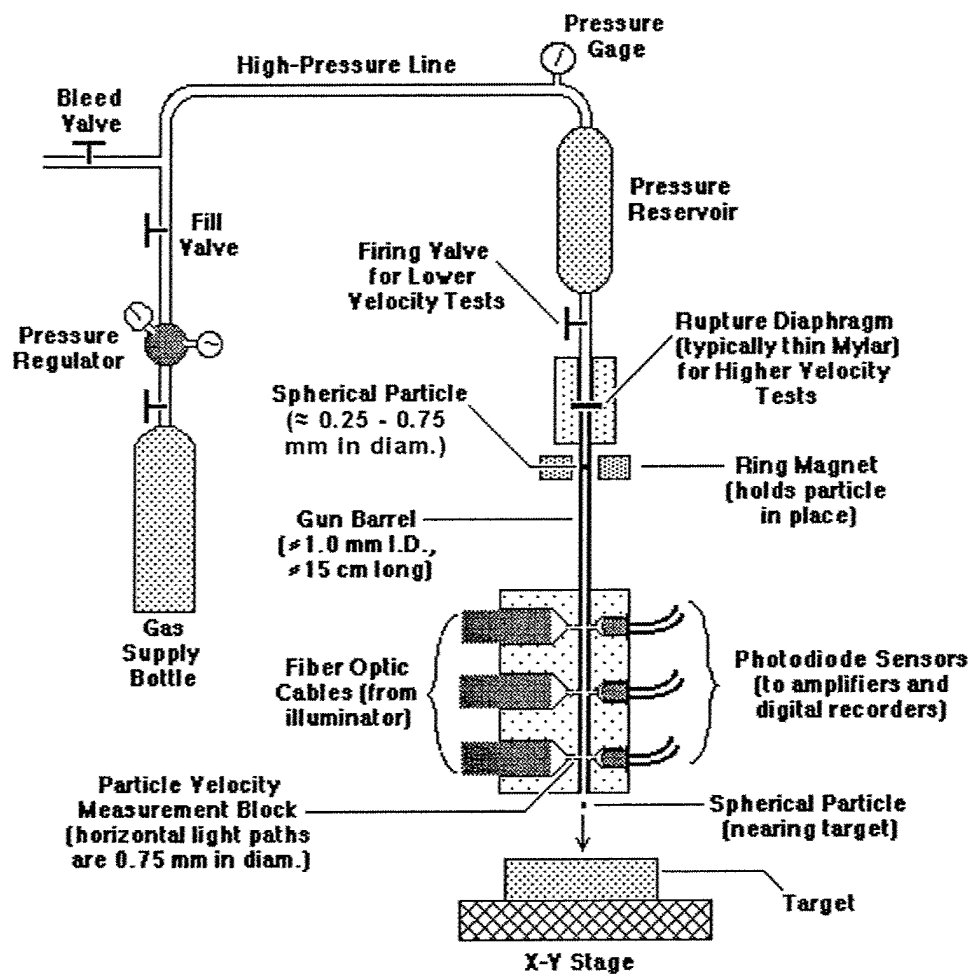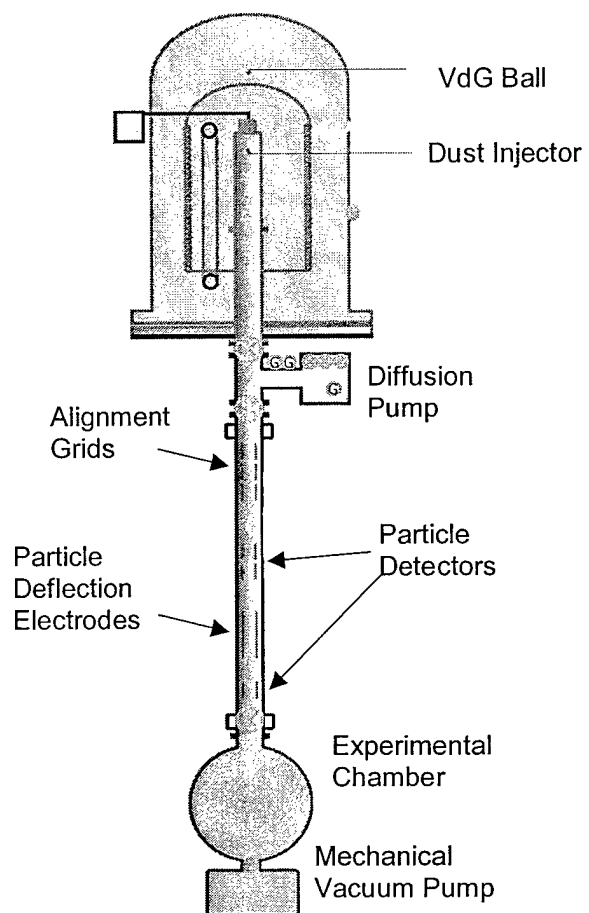
Figure 2

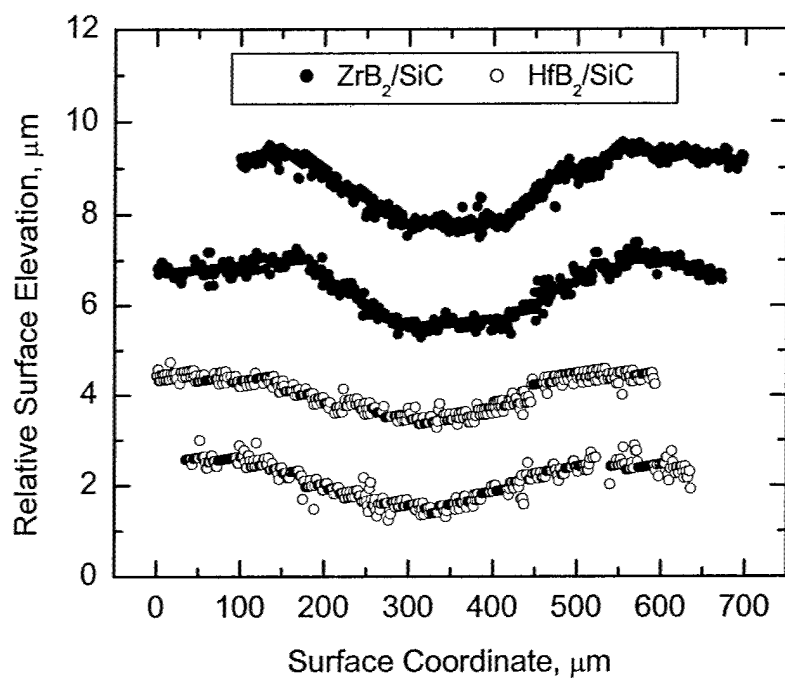*Figure 3*

Figure 4

Figure 5

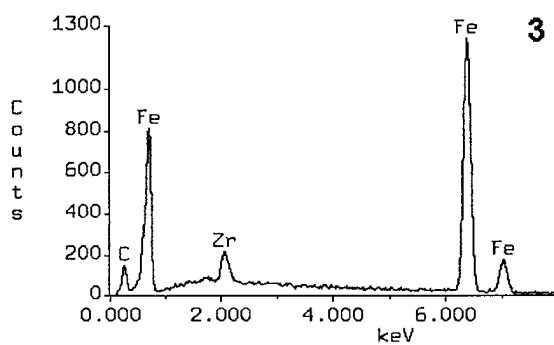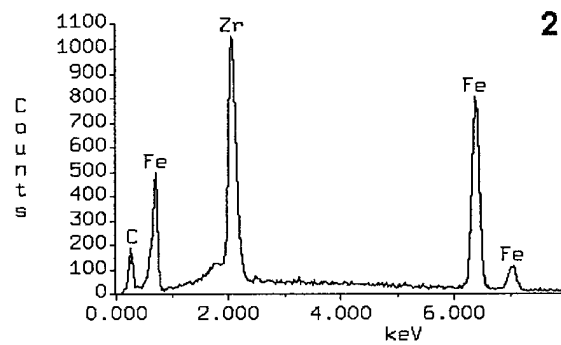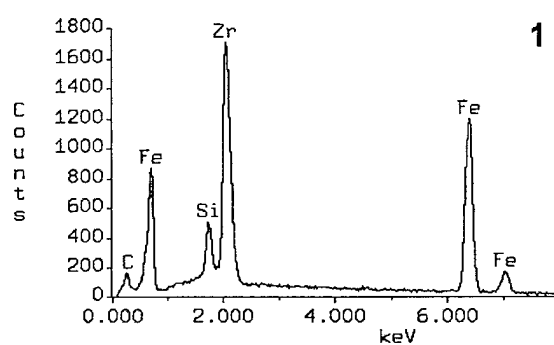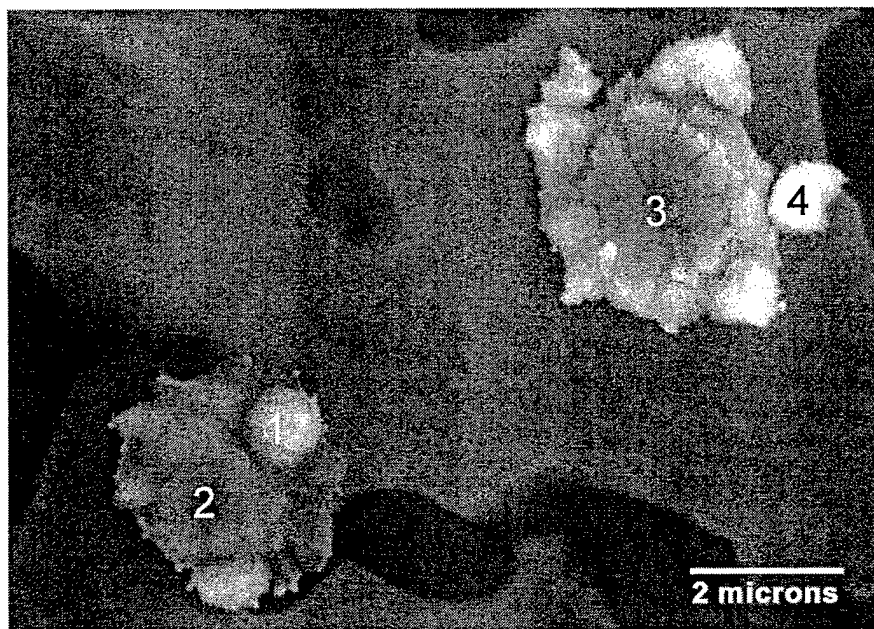*Figure 6*

Figure 7

200 microns
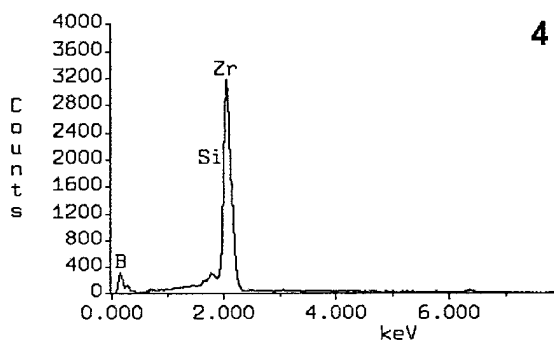
Figure 8

Figure 9

Figure 10

References

1. D. SAUNDERS, G. ALLEN, P. GAGE and J. REUTHER, "Crew Transfer Vehicle Trajectory Optimization", AIAA Paper 2001-2885, June 2001.

2. J. REUTHER, D. KINNEY, S. SMITH, D. KONTINOS, P. GAGE and D. SAUNDERS, "A Reusable Space Vehicle Design Study Exploring Sharp Leading Edges", AIAA Paper 2001-2884, June 2001.

3. K. UPADHYA, J.-M. YANG and W. P. HOFFMAN, *The American Ceramic Society Bulletin* **76** (1997) 51.

4. L. KAUFMAN, "Boride Composites - A New Generation of Nose Cap and Leading Edge Materials for Reusable Lifting Re-entry Systems", AIAA Paper 70-278, February 1970.

5. E. V. CLOUGHERTY, R. L. POBER and L. KAUFMAN, *Transactions of the Metallurgical Society of AIME* **242** (1968) 1077.

6. W. C. TRIPP, H. H. DAVIS and H. C. GRAHAM, *Ceramic Bulletin* **52** (1973) 612.

7. J. BULL. in *19th Conference on Composite Materials and Structures* 157 (CIAC, Cocoa Beach, FL, 1995).

8. A. G. METCALFE, N. B. ELSNER, D. T. ALLEN, E. WUCHINA, M. OPEKA and E. OPILA, *Electrochemical Society Proceedings* **99-38** (1999) 489.

9. I. G. TALMY, J. A. ZAYKOSKI and M. A. OPEKA, *Ceramic Engineering and Science Proceedings* **19** (1998) 104.

10. P. KOLODZIEJ, J. BULL, J. SALUTE and D. L. KEESE, "First Flight Demonstration of a Sharp Ultra-High Temperature Ceramic Nosetip", NASA TM-112215, December 1997.

11. J. BULL, P. KOLODZIEJ, J. SALUTE and D. KEESE, "Design, Instrumentation and Preflight Testing of a Sharp Ultra-High Temperature Ceramic Nosetip", NASA TM-1998-112229, October 1998.

12. T. KOBAYASHI and D. A. SHOCKEY, *Advanced Materials and Processes* **140** (1991) 28.

13. ANON., "Standard Test Method for Monotonic Equibiaxial Flexural Strength of Advanced Ceramics at Ambient Temperature", ASTM C 1499-03, July, 2003.

14. B. LAWN and R. WILSHAW, *Journal of Materials Science* **10** (1975) 1049.

15. A. G. EVANS and T. R. WILSHAW, *Acta Metallurgica* **24** (1976) 939.

16. D. R. CLARKE and K. T. FABER, *Journal of Physics and Chemistry of Solids* **48** (1987) 1115.

17. B. R. LAWN and M. V. SWAIN, *Journal of Materials Science* **10** (1975) 113.

18. B. R. LAWN, T. JENSEN and A. ARORA, *Journal of Materials Science Letters* **11** (1976) 573.

19. B. R. LAWN and E. R. FULLER, *Journal of Materials Science* **10** (1975) 2016.

20. A. G. EVANS, *Journal of the American Ceramic Society* **56** (1973) 405.

21. B. R. LAWN, S. M. WIEDERHORN and H. H. JOHNSON, *Journal of the American Ceramic Society* **58** (1975) 428.

22. C. G. KNIGHT, M. V. SWAIN and M. M. CHAUDHRI, *Journal of Materials Science* **12** (1977) 1573.

23. S. M. WIEDERHORN and B. R. LAWN, *Journal of the American Ceramic Society* **60** (1977) 451.

24. W. H. RHODES, E. V. CLOUGHERTY and D. KALISH, "Research and Development of Refractory Oxidation-Resistant Diborides, Part II, Volume IV: Mechanical Properties", AFML-TR-68-190, January 1970.

25. V. E. LYSAGHT and A. DEBELLIS, "Hardness Testing Handbook" (American Chain and Cable Company, 1969).

26. Y. V. MILMAN, B. A. GALANOV and S. I. CHUGUNOVA, *Acta Metallurgica et Materialia* **41** (1993) 2523.

27. L. BSENKO and T. LUNDSTRÖM, *Journal of the Less-Common Metals* **34** (1974) 273.

28. K. NAKANO, H. MATSUBARA and T. IMURA, *Journal of the Less-Common Metals* **47** (1976) 259.

29. V. M. GLAZOV and V. N. VIGDOROVICH, "Microhardness of Metals and Semiconductors" (Consultants Bureau, New York, 1971).

30. G. D. QUINN, P. J. PATEL and I. LLOYD, *Journal of Research of the National Institute of Standards and Technology* **107** (2002) 299.

31. A. KAKANAKOVA-GEORGIEVA, E. P. TRIFONOVA, R. YAKIMOVA, M. F. MACMILLAN and E. JANZÉN, *Crystal Research and Technology* **34** (1999) 943.